Retrieval and Validation of Total Seasonal Liquid Water Amounts in the Percolation Zone of Greenland Ice Sheet Using L-band Radiometry

Alamgir Hossan[1], Andreas Colliander[1], Baptiste Vandecrux[2], Nicole-Jeanne Schlegel[3], Joel Harper[4], Shawn Marshall[5], Julie Z Miller[6]

[1]Jet Propulsion Laboratory, California Institute of Technology
[2]Geological Survey of Denmark and Greenland
[3]NOAA/OAR Geophysical Fluid Dynamics Laboratory (GFDL)
[4]Department of Geosciences, University of Montana
[5]Department of Geography, University of Calgary
[6]Cooperative Institute for Research in Environmental Sciences, University of Colorado Boulder

Correspondence to: Alamgir Hossan (alamgir.hossan@jpl.nasa.gov) and Andreas Colliander (andreas.colliander@jpl.nasa.gov)

Abstract. Quantifying the total liquid water amounts (LWA) in the Greenland ice sheet (GrIS) is critical for understanding GrIS firn processes, mass balance, and global sea-level rise. Although satellite microwave observations are very sensitive to ice sheet melt and thus can provide a way of monitoring the ice sheet melt globally, estimating total LWA, especially the sub-surface LWA, remains a challenge. Here, we present a microwave retrieval of LWA over Greenland using enhanced resolution L-band brightness temperature (TB) data products from the NASA Soil Moisture Active Passive (SMAP) satellite for the 2015-2023 period. L-band signals receive emission contributions deep in the ice sheet and are sensitive to the liquid water content (LWC) in the firn column. Therefore, they can estimate the surface-to-subsurface LWA, unlike higher frequency signals (e.g., 18 and 37 GHz bands), which are limited to the top few centimeters of the surface snow during the melt. We used vertically polarized TB (V-pol TB) with empirically derived thresholds to detect liquid water and identify distinct ice sheet zones. A forward model based on radiative transfer in the ice sheet was used to simulate TB. The simulated TB was then used in an inversion algorithm to estimate LWA. Finally, the retrievals were compared with the LWA obtained from two sources. The first source was a locally calibrated ice sheet energy and mass balance (EMB) model, and the second source was the Glacier Energy and Mass Balance (GEMB) model within the National Aeronautics and Space Administration's (NASA) Ice-sheet and Sea-Level System Model (ISSM). Both models were forced by *in situ* measurements from six automatic weather stations (AWS) of the Programme for Monitoring of the Greenland Ice Sheet (PROMICE) and Greenland Climate Network (GC-Net) located in the percolation zone of the GrIS. The retrievals show generally good agreement with both the references,

demonstrating the potential for advancing our understanding of ice sheet physical processes to better project Greenland's contribution to the global sea level rise in response to the warming climate.

1 Introduction

Continuous mass loss of the Greenland Ice Sheet (GrIS) has been a significant concern in the context of climate change and associated sea level rise (Khan et al., 2015; Mouginot et al., 2019; Otosaka et al., 2023; Shepherd et al., 2020). Greenland has lost about 330 billion tons of mass, equivalent to around 1 mm global sea level rise, per year on average for the last two decades (Greene et al., 2024; Khan et al., 2022). This will likely accelerate in the coming decades, even with the most optimistic warming scenario.

Mass loss occurs through surface melt and the subsequent runoff of meltwater towards the ice sheet margin and solid ice discharge (calving) at marine-terminating outlet glacier termini. While meltwater runoff has been the dominant contributor to mass loss in Greenland, both have increased in the last few decades (Van Den Broeke et al., 2016; Greene et al., 2024; Mouginot et al., 2019; Vandecrux et al., 2023a). In the ablation area, the winter snowpack is melted out every summer and the meltwater enter an efficient drainage network of streams and lakes toward the margin (Smith et al., 2017). Higher up on the ice sheet, in the accumulation area, there is less melt, and a porous snow layer accumulated over the years, called firn, leads to the percolation and refreezing of surface melt, buffering additional sea level rise (Harper et al., 2012; Samimi et al., 2020). However, with intense and frequent melt events, thick ice layers, called ice slabs, are formed from meltwater refreezing, impeding vertical percolation of meltwater and promoting horizontal runoff (Culberg et al., 2021; Jullien et al., 2023; MacFerrin et al., 2019; Miller et al., 2022b, 2020b; Tedstone and Machguth, 2022). Increased refreezing resulted in a loss of approximately 5% of GrIS firn air content (FAC) between 1996 and 2019 (Medley et al., 2022). These effects gradually diminish the ice sheet's inherent capability to retain meltwater and buffer sea level rise (Harper et al., 2012; Mikkelsen et al., 2016; Vandecrux et al., 2019).

Furthermore, increased melting contributes to forming supraglacial, englacial, and subglacial meltwater features (e.g., lakes, rivers, slush, crevasses, moulins, and firn aquifers, etc.) that can augment dynamical discharge and calving losses by lubricating the basal sliding surface and accelerating the flow of outlet glaciers (Hoffman et al., 2011; Schoof, 2010; Sundal et al., 2011; Zwally et al., 2002). Therefore, meltwater not only contributes to sea-level rising through direct runoff, but it can also alter the physical structure that governs the dynamics and evolution of the ice sheet. Hence, quantification of total surface and subsurface liquid water is essential to understand ice sheet response to climate changes and project sea level rise accurately.

Surface melt and liquid water amount (LWA) can be estimated with various techniques. *In situ* AWS networks provide meteorological observations (Fausto et al., 2021), which can drive surface energy and mass balance (EMB) models to derive surface melt and LWA. Other *in situ* measurements such as upward-looking radar (Heilig et al., 2018) or time domain resistivity probes(Samimi et al., 2021) can also be used to measure LWA at a given site. Due to logistical constraints, these point observations have a limited spatial and temporal coverage.

Regional climate models (RCM) are primarily used to estimate ice sheet-wide LWA, surface mass balance (SMB), and their changes (Fettweis et al., 2020). The results of RCMs are difficult to validate on the scale of the ice sheet, given the scarcity of *in situ* data to constrain and calibrate these models. Moreover, diversity exists in representation of the surface and sub-surface firn processes among RCMs, leading to significant uncertainties in LWA estimates and their temporal and spatial variabilities (Fettweis et al., 2020; Thompson-Munson et al., 2023; Vandecrux et al., 2020; Verjans et al., 2019).

Satellite-based observations, especially microwave sensors, are very sensitive to ice sheet melting, manifested by large changes in dielectric constant with liquid water and can provide global coverage in day-night and all-weather conditions (Abdalati and Steffen, 1997; Mote and Anderson, 1995; Picard et al., 2022; Tedesco, 2007; Tedesco et al., 2007; Zwally and Fiegles, 1994). Accordingly, both active (radars) and passive sensors (radiometers) have been used to monitor surface melting across Greenland and Antarctica ice sheets (Abdalati and Steffen, 1995, 2001; Hall et al., 2009; Mote, 2007; Nghiem et al., 2001; Tedesco, 2007; Wismann, 2000; Zwally and Fiegles, 1994). However, these conventional approaches applying high-frequency bands (i.e., 18 and 36 GHz) from the legacy and operational radiometers (Abdalati and Steffen, 1997; Ashcraft and Long, 2006; Colosio et al., 2021; Fettweis et al., 2007, 2011; Tedesco, 2007, 2009; Tedesco et al., 2007; Zwally and Fiegles, 1994) can only track the surface and near-surface binary melt status, not the meltwater propagation into the deeper layers because of their limited penetration depth and sensitivity to LWC (Colliander et al., 2022a, b, 2023; Mousavi et al., 2022). The emergence of L-band (1 - 2 GHz) radiometry, marked by the launch of ESA's Soil Moisture and Ocean Salinity (SMOS) mission (November 2009 - present) and the collaborative effort between NASA and Argentina's space agency CONAE in the Aquarius mission (October 2011 - June 2015), followed by NASA's Soil Moisture Active Passive (SMAP) mission (March 2015 - present), has opened up the possibilities for monitoring ice sheet meltwater at greater depths. L-band signals can penetrate deeper and provide a more accurate estimate of sub-surface liquid water (Colliander et al., 2022b; Miller et al., 2020a, 2022a, b; Mousavi et al., 2022). Nevertheless, only a few attempts have been made to quantify the amount of liquid water (Colliander et al., 2022a; Houtz et al., 2019, 2021; Mousavi et al., 2021; Schwank and Naderpour, 2018).

Houtz et al. (2019) used the SMOS multi-angle L-band radiometric observations with a two-layer configuration of the L-band specific Microwave Emission Model of Layered Snowpacks (LS-MEMLS) model (Schwank et al., 2014) in an inversion-based retrieval framework for simultaneous estimation of snow liquid water content and density at the Swiss Camp site located in the ablation zone of the western Greenland ice sheet (GrIS). This initial study evaluated the results with in situ air temperature and another satellite-based empirical melt detection algorithm, called the XPGR (the cross-polarized gradient ratio of 19 GHz and 37 GHz TBs) (Abdalati and Steffen, 1995, 1997); however, it did not include any in situ validation of actual LWA. Naderpour et al. (2021) supported Houtz et al. (2019) findings using a close-range (CR) single-angle L-band microwave radiometer measurements and the same L-band specific forward model (LS-MELMS) at the Swiss Camp location. Houtz et al. (2021) extended the Houtz et al. (2019) approach to estimate LWA over the entire GrIS where they tuned the wet layer thickness (10 cm – 100 cm) to provide variable estimates of liquid water which also were not validated against any reliable reference. Field observations and modelling results provide evidence of meltwater infiltration for more than 100 cm, especially in the percolation zone of the GrIS (e.g., Samimi et al. 2021; Vandecrux et al., 2020). Mousavi et al. (2021)

developed an L-band specific snow/firn radiative transfer model to derive multidimensional brightness temperature look up tables for the frozen and melt season considering a four-layer ice sheet structure. The algorithm uses frozen season brightness temperature to determine the baseline emissions (temperature, density, scattering coefficient) which are then used in melt season to estimate liquid water content and corresponding wet layer thickness. In this paper, we extend Mousavi et al., (2021) approach with improved and updated LUT to quantify and validate the LWA with two state-of-the-art surface energy balance models forced with in situ observations, and to examine their spatial and temporal variability.

2 Methods

2.1 SMAP L-band Enhanced Resolution Brightness Temperatures

SMAP was launched on January 31, 2015, and has been operational since March 31, 2015 (Entekhabi et al., 2010). It was placed in a 685-km altitude and 98.1◦ inclination sun-synchronous polar orbit with 6 AM/6 PM equator-crossing. It carries a conically scanning radiometer operating at 1.41 GHz (L-band) with a constant incidence angle of 40◦ that results 1000-km wide swath giving twice daily coverage of GrIS. It measures brightness temperature (TB) in fully polarimetric mode giving the horizontal and vertical polarizations, as well as the 3rd and 4th Stokes parameters with native 38-km spatial resolution. The radiometric precision of the SMAP radiometer is within 0.5 K (Chaubell et al., 2018, 2020; Piepmeier et al., 2017). For Jun 20 – July 23, 2019, and Aug 6 - Oct 16, 2022, SMAP does not have results because of an operational outage of the satellite.

Here, we used SMAP L-band enhanced-resolution TB products generated using the radiometer form of the Scatterometer Image Reconstruction (rSIR) algorithm and projected on the EASE-2 3.125 km grid (Brodzik et al., 2021; Long et al., 2019). The rSIR algorithm leverages the measurement response function (MRF) of each observation and combines the overlapping MRFs to reconstruct enhanced-resolution TB images. The effective resolution of SMAP enhanced-resolution TB products posted on a 3.125 km grid is ~30 km compared to the 46 km effective resolution of the SMAP original data products (Long et al., 2023). Therefore, it improves the overall effective resolution of about 30% compared to coarser grid postings (Long et al., 2023; (Zeiger et al., 2024). The data product provides two TB images daily – the morning and evening facilitating the resolution of diurnal variability. The spatial oversampling and resolution enhancement enables an improved characterization of spatial heterogeneity (Long et al., 2023). The land–ocean mask used to locate the ice sheet edge comes from PROMICE (Citterio and Ahlstrøm, 2013).

2.2 Microwave Radiometric Response of GrIS

2.2.1 Theoretical Background

Microwave radiometers measure the naturally emitted thermal radiation, called the brightness temperature (TB), by the firn as observed in the microwave portion of the electromagnetic spectrum. It is related to the emissivity e and the effective physical

128   temperature T_{phy} of snow/firn/ice media for a given frequency f, polarization p, and incidence angle θ. If firn were vertically

129   homogeneous or isothermal, the TB could be found according to Rayleigh-Jeans approximation (Ulaby and Long, 2014):

130     $T_B(f, p, \theta) = e\, T_{phy}$ (1)

131   However, firn is not a vertically homogenous medium. Both the emissivity and temperature vary with depth. As a

132   result, the TB is given by a depth-integrated product of physical temperature and emissivity, weighted by the emissive,

133   absorptive, and scattering properties of the snow/firn/ice layers (Jay Zwally, 1977) which is strongly dependent on the

134   frequency of observation.

135   To account for the depth dependencies of snow and ice properties, firn is considered as a complex multilayer dense

136   medium. For each layer, an effective physical temperature and permittivity is determined from firn absorptive and scattering

137   properties. Then the microwave emission and its propagation are typically modeled using equation of radiative transfer (RT).

138   Considering firn as a stack of N plane-parallel layers consisting of isotropic and homogeneous material in each layer, the RT

139   equation can be given as (Jin, 1994, 1997; Picard et al., 2013; Tsang et al., 2000):

140     $\cos\theta \dfrac{d}{dz}\boldsymbol{T_B}(z,\theta,\emptyset) = \kappa_a \boldsymbol{T}(z)\boldsymbol{I} - \kappa_e \boldsymbol{T_B}(z,\theta,\emptyset) + \int_0^{\frac{\pi}{2}} \int_0^{2\pi} \sin\theta'\, d\theta' d\emptyset' \boldsymbol{P}(\theta,\emptyset,\theta',\emptyset')\boldsymbol{T_B}(z,\theta',\emptyset')$ (2)

141   Here, $\boldsymbol{T_B}(z,\theta,\emptyset)$ denotes the vertically and horizontally polarized brightness temperatures at depth z propagating along a

142   direction characterized by θ (zenith angle) and ϕ (azimuth angle). κ_e, κ_a, and κ_s are the extinction, absorption, and scattering

143   coefficients, respectively, representing medium properties. For an isotropic medium, the extinction coefficient can be described

144   as, $\kappa_e = \kappa_a + \kappa_s$. θ' and ϕ' are slant angles and $\boldsymbol{P}$ is bistatic scattering phase function. $\boldsymbol{T}(z)$ is the physical temperature of

145   snow at depth z, and $\boldsymbol{I}$ is a unit vector. Thus, the first term on the right-hand side of Eq. 2 represents the microwave emission

146   (T_B) of snow/fir/ice from depth z, and the second term denotes the extinction (attenuation) of the emission due to absorption

147   and scattering. The third term represents the sum of total scattered emission in the direction of the receiver (as specified by θ

148   and ϕ). Eq. 2 is solved analytically or numerically subject to boundary conditions at each layer interface and at the top and

149   bottom of the medium

150   The extinction coefficient, κ_e is function of the effective dielectric constant of the layer and frequency of the

151   observation. Thus, the overall TB is given by the depth-integrated profiles of the effective physical temperature and dielectric

152   constant of each layer. So, penetration depth plays a key role in determining the variability of TB, especially in low-frequency

153   bands. For a low-loss media like firn, the penetration depth can be approximated as (Elachi and Zyl, 2021):

154     $\delta = \dfrac{c\sqrt{\epsilon'}}{2\pi f \epsilon''}$ (3)

155   where c is the speed of light and, ϵ' and ϵ'' are the real and imaginary parts of the dielectric constant of the firn. As shown, δ

156   is inversely proportional to both, f and ϵ''. L-band signal thus penetrates a significantly thicker layer than the higher frequency,

157   like Ka-band signal. Liquid water markedly increases ϵ'' (compared to $\sqrt{\epsilon'}$ in proportion), decreasing the penetration depth for

any frequency. For a typical snow density (measured for dry snow) in the percolation zone, it can be more than 4 m for an average LWC of less than 1% with the Ulaby and Long (2014) model's wet snow dielectric constant, decreasing exponentially with the LWC. Thus, for an average LWC of 3% and higher, it is around 1 m and less. The average LWC in the percolation zone is typically not higher than 4%, except for extraordinary melt years (like 2012, not included in the study), and typical infiltration of liquid water is also generally within upper 4 m (Samimi et al., 2020, 2021).

There are two types of scattering processes in the snow/firn medium affecting the propagation: surface scattering and volume scattering. The relative size of the scatterers compared to the wavelength determines the degree and types of scattering. For high frequency bands (>10GHz), the impact of volume scattering is critical because the fractional volume of scatterers (snow/firn) is significant. This is why the high-frequency signals interact more with fresh snow, grain size, and roughness at the surface. Low-frequency signals (<10GHz) are relatively insensitive to volume scattering from snow grains because the size of the scatterers is much smaller than the wavelength. Surface scattering occurs due to surface irregularities at the interface between layers of different dielectric constants, affecting all the frequencies when present. Horizontal and vertical ice layers (strata) are formed at various depths in the firn primarily from the refreezing of seasonal snow melts. Over time, older ice layers move downward due to the snow accumulation while new ice layers are formed for subsequent melts at the top layers, creating a complex set of stratigraphy and significantly influencing the L-band signals from the deeper layers. Therefore, L-band TB is determined by the subsurface temperature, stratigraphy, and LWA.

2.2.2 Frozen Season Response

L-band TB exhibit some distinct spatial features over GrIS during a frozen season. Along a typical west-east transect, TB is the highest in the ablation zone, then it gradually decreases to its lowest value in the percolation zone, followed by a gradual increase towards a moderate value in the upper accumulation zone. A mirror image is seen on the eastern side of the ice sheet. The spatial features of H-pol TB are similar to V-pol TB, but it is more affected by sub-surface layering. This is illustrated in Figure 1 with V- and H-pol mean frozen season TBs and their normalized polarization ratio (NPR, defined as NPR = (TBV-TBH)/(TBV+TBH)). The ablation zone is characterized by exposed glacial ice with a high density and internal temperature than those of the ice sheet towards Greenland's interior. It is soaked and swept by a large amount of meltwater every year. During the frozen season, the L-band emission has a high effective emissivity, radiating the warmer physical temperature of the deeper layers. In the percolation zone, on the other hand, moderate, but varying melt occurs almost each or every few years that percolates down and refreezes at different depths forming discrete ice layers and ice pipes, causing substantial scattering of mean TB (Jezek et al., 2018). High NPR values highlight the area with dense ice layers (strata). The upper accumulation zone experiences light or no melt but accumulates snow, resulting in less density variation compared to the percolation zone. For detecting melt and quantifying LWA, we used vertically polarized TB (V-pol TB) considering its lower sensitivity to sub surface stratigraphy.

V-pol TB (TBV)   **H-pol TB (TBH)**   **(TBV - TBH)/(TBV + TBH)**

(a)   (b)   (c)

190
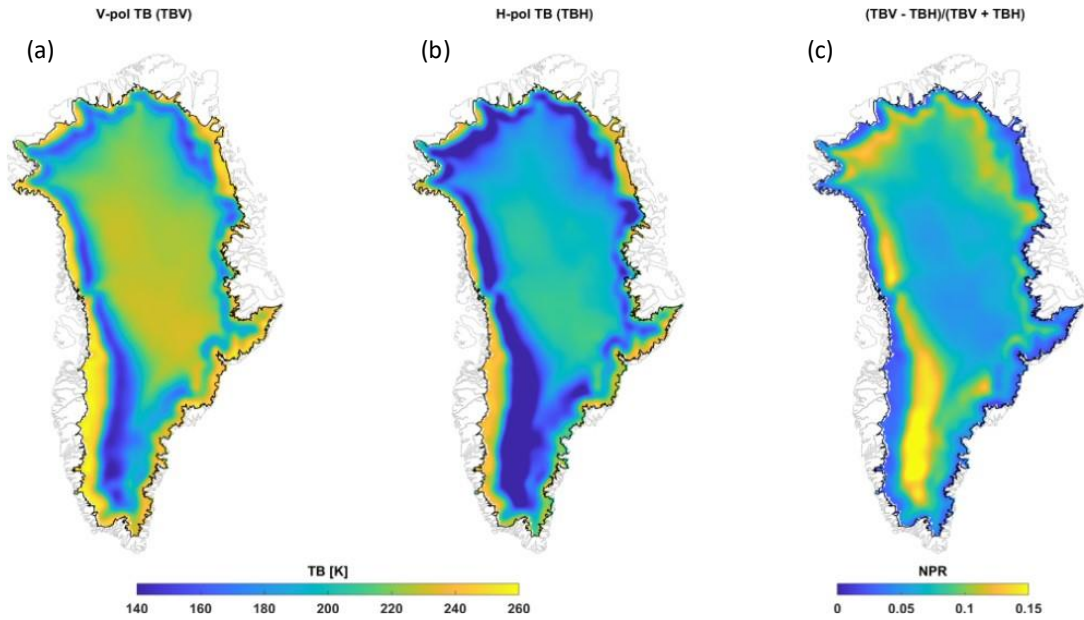
191   **Figure 1: L-band radiometric response of GrIS during frozen season. Vertically polarized TB (a), horizontally polarized TB (b)**
192   **averaged over Jan 1 – Apr 7th, 2015 – 2023, and their normalized polarization difference (c).**

193   **2.2.3 Melt Season Response**

194   During summer season in presence of melt, the L-band TB generally decreases in the ablation and upper accumulation zones
195   compared to the frozen season, while it increases significantly in the percolation zone. Fig. 2 illustrates this for a sample
196   summer day (Jul 31, 2019) when melt was detected across the K-transect (~ 67° constant latitude; see the red line in Figure
197   2a). The melt flags (square symbols over dashed line) specify the TB samples for which melt was detected (Sec. 3.2). The
198   presence of LWC in the snow and firn increases the absorption and emission in turn (Mote and Anderson, 1995). However, at
199   the lower elevation around the ablation zone, the TB decreases from its very high level (~260 K) as the LWC of the seasonal
200   snow layer increases. This is because, when the LWC in the snow layer exceeds a threshold, snow becomes saturated and it
201   creates a reflective boundary at the ice and snow interface, suppressing the emission from the ice layer and resulting in overall
202   lower TB. This is caused by intense melting common in the ablation zone (Figure 2b). The percolation zone experiences
203   moderate melt, making the snow and firn highly absorptive during melt season. As a result, the TB gradually increases from
204   its winter references (Figure 2b), making the L-band sensitive to the total amounts of melt. In the upper accumulation zone,
205   melt seldom occurs. But when it occurs, it may percolate and refreezes quickly in the colder snow creating ice layers that cause
206   reflection, reducing L-band TB signals.

207

208
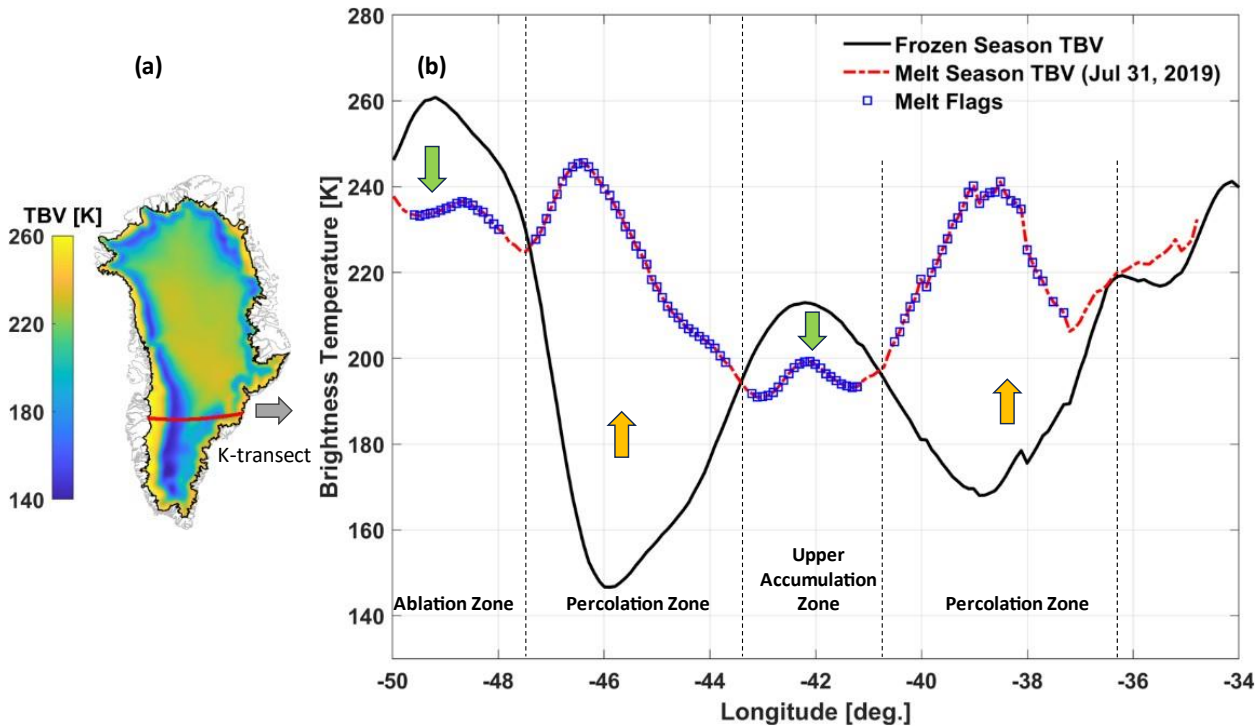
Figure 2: Radiometric response of L- band TB during frozen and melt season. The location of K-transect is highlighted by red line over the mean frozen season TBV map (a). Corresponding TBs across the transect are shown in (b): the black line represents the mean V-pol TB during the frozen season (Jan 1 – Apr 7th of the same year). The red dash-dotted line indicates TB responses on a sample melt day (Jul 31, 2019). The blue square symbols on the red dashed-dotted line depict melt flags (melt detections). Approximate location of ablation, percolation, and upper accumulation zones are depicted along the K-transect for reference.

Figure 3 shows the L-band V-pol TB time series during Mar – Oct 2016 at the DY2 AWS, a location representative of the percolation zone. During the frozen season, the L-band TB is relatively lower and stable. During the melt season, it captures the diurnal signals during melting phases (melt generation). However, it diminishes as the melt percolates to deeper layers. From the onset through the end of the melt season, the density and grain size increase in the snow and firn layers due to melt (Vandecrux et al., 2022). Although the L-band TB is relatively insensitive to the grain growth, the post-melt TB level may still decrease because of increased reflection from newly formed ice layers. This effect is pervasive, especially across the accumulation zone justifying a dynamic threshold in threshold-based melt detection algorithms.

221
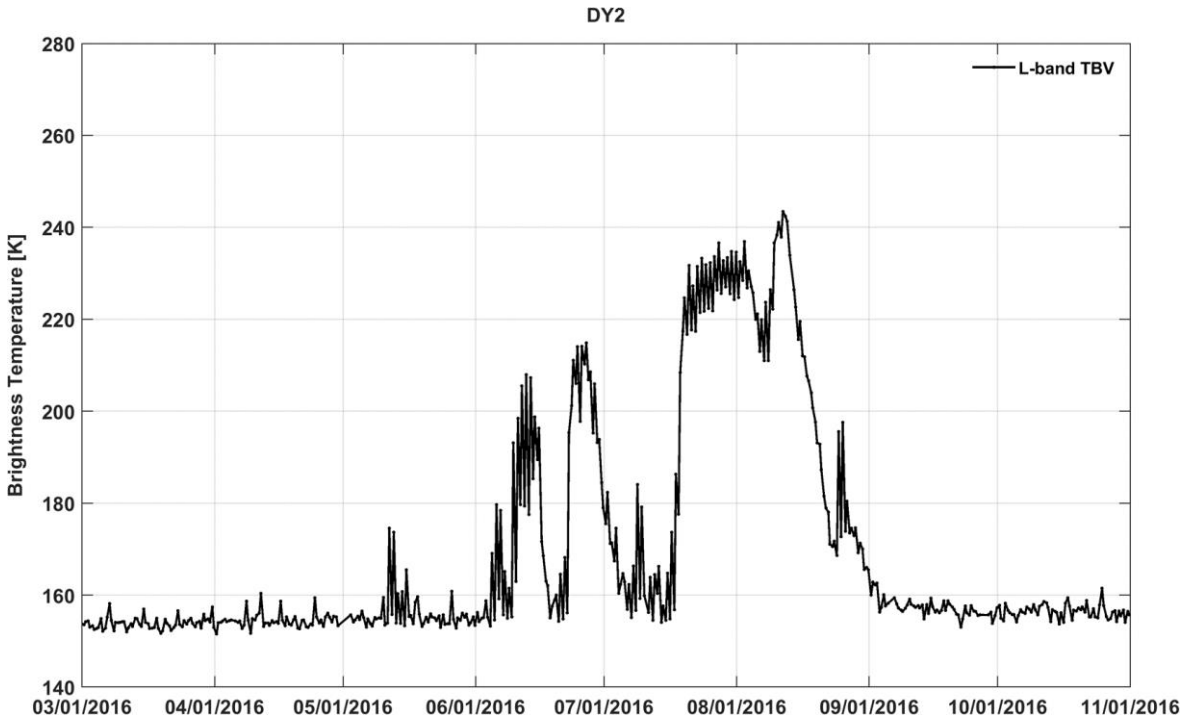
222 **Figure 3: L- band V-pol TB time series at the DY2 automatic weather station location during** during Mar – Oct, 2016 **illustrating**

223 **the change of TB level caused by melting, snow accumulation, and other physical processes.**

224 **2.3 Melt Retrieval Algorithm**

225 We used a threshold-based empirical detection algorithm to detect surface and subsurface melt events. The threshold is

226 determined by:

227 $T = \mu \pm m\sigma$ (4)

228 where μ is a reference TB (the mean during the frozen season), σ is the standard deviation of the TB during the reference

229 period, and m is an empirically derived constant. A constant value of 10 was chosen for m. First, to detect the first and last

230 melt during a year for a grid point, mean TB during Jan 1 – Apr 7th, and October 24 – December 31 was used as the reference

231 values, respectively. Jan 1 – Mar 31 is generally considered fully frozen conditions regardless of elevation and latitudes. SMAP

232 does not have data for Jan 1 – Mar 30, 2015, because the data production started on March 31, 2015; therefore, we extended

233 the reference period to Apr 7th for all the years to make it consistent. October 24 – December 31 was determined based on

234 visual observations of the time series during 2015-2023. An averaged value of σ_{spring} and σ_{fall} is used with final adjustment

235 of m in such a way that the threshold does not miss the first and last melts. Then a linearly transitional reference value is used

236 between the first and last melt days to account for the change in TB value for subsequent melt because of refreezing.

237   We used an inversion of a simplified ice sheet emission model to estimate the LWA and physical properties of the

238   detected melt events. The retrieval algorithm consists of a forward model (Fig. 4) simulating the L-band TB (Mousavi et al.,

239   2021) and a cost function minimization between the simulated and observed TB. The forward model represents the ice sheet

240   as a stack of 4 vertical layers, where each layer is characterized by its complex dielectric constant (ϵ), density (ρ), physical

241   temperature (T), and thickness (d). The top layer is air above the snow and assumed to be semi-infinite (surface to radiometer

242   antenna) and the bottom layer (Layer 3 in Fig. 4) is also assumed semi-infinite, while the intermediate layers are configured

243   with variable thicknesses. The first snow/firn layer (Layer 1 in Fig. 4) holds dry and wet snow/firn during frozen and melt

244   seasons respectively. To account for the combined reflective effects by the complex stratigraphy due to numerous ice layers

245   common in the percolation zone of the GrIS, as well as the effects of multiple scattering in the snow/firn layer, we designate

246   Layer 2 (underneath the dry/wet snow/firn layer) as a highly reflective layer by explicitly specifying its dielectric constant

247   (with high real part that varies spatially). The TB is then modelled using the incoherent approach of radiative transfer (RT)

248   theory, without considering the effects of volume scattering analytically (but considering its dielectric effects explicitly). For

249   a specific depth z, the upwelling TB, for a given polarization, p, is given by:

250    $$T_{Bnp}^u(\theta_n, z) = \left[\Gamma_{np} T_{Bnp}^d(\theta_n, - d_n) + (1 - \Gamma_{np})T_{B(n+1)p}^u(\theta_{(n+1)}, - d_n)\right]e^{-k_{an}(z+d_n)\sec\theta_n} + (1 - e^{-k_{an}(z+d_n)\sec\theta_n}) T_n$$

251    $$(5)$$

252   where T_{Bnp}^u and T_{Bnp}^d represents the upwelling and downwelling p-polarized TB at the interface z = - d_n characterized by

253   reflectivity Γ_{np}. θ_n is the incidence angle determined from the Snell's law and dielectric constant, and k_{an} is the power

254   absorption coefficient given by k_{an} = - $2\text{Re}\{ \omega\sqrt{\varepsilon_n\mu_0} \}$, where ω is the angular frequency, ε_n is the complex permittivity of

255   the layer, and μ_0 is the magnetic permeability for a nonmagnetic material. T_n is the physical temperature of the layer and

256   assumed to be homogenous within the layer. The downwelling part of the TB, $T_{Bnp}^d(\theta_n, - d_n)$, is given by:

257    $$T_{Bnp}^d(\theta_n, - d_n) = \Gamma_{(n-1)p} T_{Bnp}^u(\theta_n, - d_{n-1}) + (1 - \Gamma_{(n-1)p}) T_{B(n-1)p}^d(\theta_{(n-1)}, - d_{n-1}) \qquad (6)$$

258   It is assumed that there are no downward and upward emissions beyond the top and bottom semi-infinite layers

259   respectively, and the atmospheric attenuation is also to be negligible considering L-band frequency. Therefore, the top-of-the

260   atmosphere TB is found from equation (1),

261    $$T_{BP}(\theta_0, H) \approx T_{B0p}^u(\theta_0, 0) = (1 - \Gamma_{0p}) T_{B1p}^u(\theta_1, 0) \qquad (7)$$

	(Air)	ϵ_0, T_0	(Semi-infinite)
			$z = 0$
Layer 1	(Dry/Wet Snow)	$\epsilon_1, \rho_1, T_1, d_1$	
			$z = -d_1$
Layer 2	(Highly Reflective Firn Layers)	$\epsilon_2, \rho_2, T_2, d_2$	
			$z = -d_1 - d_2$
Layer 3	(Dry Firn/Ice)	$\epsilon_3, \rho_3, T_3, d_3$	(Semi-infinite)

262

Figure 4: L-band multilayer ice sheet forward model.

For faster processing during retrieval, we developed separate look-up-tables (LUTs) for dry and melt season prescribing layer parameters by sweeping over a realistic range of each parameter. The LUTs were revised compared to their original versions (Mousavi et al., 2021) in the following way. Mousavi et al., 2021 and 2022 generated LUTs with a larger range for background temperature (110-265K)for highly reflective layer (Layer 2 in Fig. 4), and the semi-infinite ice layer (Layer 3 in Fig. 4). We used a similar procedure to derive the LUTs, but with different range and resolutions of the background parameters. For each layer, dry snow density varied from a fresh snow density of 50 kg/m^3 to that of solid ice of 917 kg/m^3. Physical temperature was prescribed from 200 K to 273.15 K. For the melt season, the wet snow layer is inserted with a volume fraction of meltwater, m_v, which is varied from 0 to 5% in 40 equally spaced steps, and thickness, d_{wet}, which is varied from 10 cm to 20 m, in 10 cm steps for the top 60 cm, 20 cm steps for next 1.4 m, 40 cm steps for next 8 m, and 1 m steps for the next 10 m. For $m_v > 0$, T_{wet} must be 0 C. Colbeck, (1974) suggested because of capillary retention, the irreducible water saturation of dense snow/firn is about 7% of its pore volume. Coléou and Lesaffre, (1998) showed that the irreducible water content can be up to 6.5 - 8.5 % of the pore volume depending on the density. Based on these studies and considering snow/firn density in the percolation zone, we determined the maximum volume fraction to be 5%. The dielectric constant of the dry snow was calculated using Mätzler (2006), and wet snow following Ulaby and Long (2014). Ulaby and Long (2014) model of wet snow dielectric constant is an empirical model, called the 'modified Debye-like model,' which is an extension of Hallikainen et al. (1986). Then, the emission model was run for each combination. The model computes the top-of-the-atmosphere L-band TB at the V- and H-pol assuming fully transparent atmosphere. With all these constraints, the tuning finally results in two LUTs with six and eight dimensions for the dry and melt seasons, respectively.

282   The inversion was performed by optimizing a cost function that minimizes the distance between the LUT-modeled
283   TB and the corresponding SMAP-measured TB for each 3.125 km grid cell. The optimization was carried out in two steps for
284   each melting grid. First, the frozen season snow/firn density, physical temperature, and dielectric constant were estimated.
285   Second, using that information, the volume fraction of meltwater m_v, and corresponding wet layer thickness d_{wet}, were
286   determined for a time stamp during the melt season. The LWA is thus the product of the two, i.e., $LWA = m_v\, d_{wet}$ [m] m.w.e.
287   This represents the instantaneous total LWA present in the SMAP footprint for that time stamp within the SMAP sensing
288   depth, covering the typical infiltration of the meltwater in the percolation zone as per the climatological records (Samimi et
289   al., 2020; Vandecrux et al., 2020). The detection algorithm uses both increasing and decreasing summer TBs (w.r.t threshold
290   T from Eq. 4) to generate melt flags; however, the inversion only considered increasing TBs for LWA quantification. We
291   averaged twice daily LWA outputs to compute daily samples.

292   **2.4 Automatic Weather Station Measurements**

293   Direct measurements of LWA are not available for validation. However, AWS networks, such as the Greenland Climate
294   Network (GC-Net) (Steffen et al., 1996; Steffen and Box, 2001) or the Programme for Monitoring the Greenland Ice Sheet
295   (PROMICE) (Fausto et al., 2021), provide essential surface parameters that can be used to estimate LWA with an energy
296   balance model. The Geological Survey of Denmark and Greenland (GEUS), now manages these two AWS networks, which
297   cumulate 33 active ice sheet sites in Greenland that provide a suite of measurements, such as incoming/outgoing short and
298   longwave radiation fluxes, snow-surface height, air temperature, air pressure, vector winds, as well as subsurface temperature
299   and density profiles (Fausto et al., 2021).

300   We used the hourly measurements from six PROMICE and GC-Net AWSs in the percolation zone to force an EMB
301   model that produce a reference LWA, which was then used to validate the LWA retrieved from SMAP observations. The
302   stations were selected considering their locations (see Fig. 5) and melt climatology. The meteorological forcing governs the
303   surface energy budget (SEB) and was used to derive a coupled energy balance and snow/firn hydrology model (Ebrahimi and
304   Marshall, 2016; Samimi et al., 2021) that provide an estimate of hourly LWC evolution within snow and firn.

305   **2.5 Ice Sheet Energy Balance and Hydrology Model**

306   The energy balance model (EBM) determines the net energy available for melt by considering the SEB along with modelled
307   surface temperature, thermal emissivity, and albedo. The coupled model also accounts for the hydrological processes like
308   meltwater infiltration, refreezing, and retention within the firn. We used two ice sheet EBMs for comparisons with the SMAP
309   LWA retrievals. A detailed description of these models is out of the scope of this article, but brief descriptions are given below.
310   Readers are referred to relevant cited articles for further details.

2.5.1 Energy Balance and Hydrology Model

A locally calibrated and validated EBM (Ebrahimi and Marshall, 2016; Samimi et al., 2020, 2021) was used as the primary reference for comparison. The EBM was initialized with ice core density profiles, stratigraphy, and the sub-surface temperature profiles (Vandecrux et al., 2023b) and forced with the hourly surface forcing from PROMICE and GC-Net AWS. The model first calculates the net energy balance from the surface forcing by combining the energy fluxes towards the surface layer. Then, it runs a subsurface model to calculate heat conduction and melt rates in the upper 20 m of the snow/firn by resolving the profile into 43 vertical layers, with gradually decreasing thickness near the surface.

When the surface temperature reaches the melting point, and the net energy is positive, melting occurs. Conversely, if net energy is negative and the surface layer is at the melting point, any existing liquid water will freeze, releasing latent heat and causing the surface layer to cool until all liquid water is refrozen, depending on the energy balance. When surface layer temperatures are below the melting point, and there is either an excess or deficit of energy leading to warming or cooling, the energy balance within a one-dimensional model of subsurface temperature evolution determines the subsurface temperature and density profiles. The model determines hydraulic conductivity and permeability after Meyer and Hewitt (2017), while thermal conductivity was modeled following Calonne et al., (2019). The profile then governs the availability of local water at any level for the next time stamp. The model relates to a basic approach to how meltwater flux percolates downward using Darcy's law. The local water balance is determined by mass conservation in each subsurface layer. Once a layer becomes temperate, it can retain liquid water within its pore space or allow it to percolate deeper (Coléou and Lesaffre, 1998). The subsurface model is coupled with a hydrology model that redistributes the meltwater; depending on the subsurface temperature profile, the meltwater may refreeze. Due to refreezing, density may increase, and ice layers may form that may reduce or completely block meltwater infiltration. The firn densification was modeled as in Vionnet et al., (2012). We henceforth refer to this model as the EBM for simplicity. To evaluate the LWA retrieval, we calculate the daily average LWA from the hourly EBM output.

2.5.2 Glacier Energy and Mass Balance (GEMB) Model

We used output from GEMBv1.0 as a secondary source of comparison. It is a module in the Ice-sheet and Sea-level System Model (ISSM, https://issm.jpl.nasa.gov/) that models the ice sheet surface-energy and mass exchange and snow/firn state in a 1D column over time (Gardner et al., 2023). It has more than 100 vertical layers with <5 cm thickness in the top layers and employs spatially variable grid size based on the ice sheet dynamics. GEMB formulates irreducible water content according to Colbeck, (1973), and uses bucket scheme (Steger et al., 2017) for liquid water infiltration. Parameterization of firn densification and thermal conductivity follow Herron and Langway, (1980) and Sturm et al., (1997) respectively. Readers are referred to Gardner et al., (2023) and references therein for further details. The model was forced with the same hourly surface forcing from PROMICE and GC-Net AWS, but gap filled with ERA5 (Hersbach et al., 2020) atmosphere and radiation conditions, after the methods described by Paolo et al., (2023). The ERA5 surface temperature and downwelling longwave

343 radiation forcing were spatially bias-corrected for each month, such that all values were adjusted by the difference between

344 the RACMO2.3 (Noël et al., 2016) and the ERA5 1980-2015 monthly means. GEMB outputs include temperature, density,

345 and LWC profiles.

346 **2.5.3 Evaluation Metrics**

347 To compare SMAP daily LWA time series with corresponding LWA from EBM and GEMB model, we considered the standard

348 evaluation metrics including mean difference, standard deviation (STD), mean absolute difference (MAD), Pearson linear

349 correlation coefficient (r), root mean square error (RMSE) for summer seasons (Jun 1 – Oct 31), 2021-2023. We also compared

350 day of melt onset (the first day of summer melt) and melt freeze up (the last day of summer melt), summer melt duration

351 (difference of melt onset and freeze up), maximum summer LWA, and annual sum of daily LWA (LWA$_{YS}$). To determine the

352 day of melt onset and freeze up, we only considered melt events with LWA > 2 mm, to avoid any spurious melts that may

353 result from any instrumental noise or other sources. The LWA$_{YS}$ is the sum of daily LWA over a year. It is a measure of the

354 total seasonal LWA, but it does not represent the total surface melt generated over a year. This is because SMAP observes the

355 instantaneous LWA, the net water balance, which is the cumulative sum of surface melt, refreezing, and runoff over SMAP

356 footprint. When the net water balance remains positive overnight, it can be considered multiple times in the total integrated

357 LWA as long as it persists.

358 **3 Results**

359 **3.1 Liquid Water Amount**

360 **3.1.1 Comparison to Locally Calibrated EBM**

361 Figure 5 shows a comparison of the SMAP-retrieved LWA with the LWA derived from the EBM at six different PROMICE

362 and GC-Net AWS sites for 2023 summer season (Jun 1 – Oct 31). The melt season at CP1 site (Figure 5a) began at the fourth

363 week of June according to both, SMAP and the EBM, and continued through the first week of September according to SMAP,

364 while it extended through the end of September in the model estimate. Shortly after complete refreezing of the first melt event

365 in late June, SMAP resumed recording LWA in first week of July. Both SMAP and the EBM closely agree in both phase and

366 magnitude of LWA during first half of July. Afterwards, the EBM reports overall higher LWA for the rest of the season and it

367 seemed to retain liquid water for an elongated period when SMAP showed a fully refrozen firn. The overall agreement is given

368 by the Pearson linear correlation coefficient (r) of 0.79 and root mean square difference (RMSD) of 19 mm. The onset of melt

369 event at KAN_U site (Figure 5b) is concurrent to CP1 in accordance with the EBM. However, SMAP did not record melt at

370 this site until the first week of July. Unlike CP1 site, SMAP reports persistent LWA through the first week of October, whereas

371 EBM shows complete refreezing by the second week of September. Both SMAP and the EBM captured less LWA at KAN_U

372 site compared to CP1. This is somewhat counter-intuitive because the KAN_U site is located at a lower elevation than CP1

site (see the elevation in Figure 5d). In fact, KAN_U is characterized by having a lower accumulation and higher melt rate every year (MacFerrin et al., 2019; Machguth et al., 2016). However, excessive melt have also created thick ice slabs in this location (MacFerrin et al., 2019; Machguth et al., 2016). As a result, liquid water cannot percolate to the deeper layers and run off horizontally. The model excludes this liquid water in the form of 'drainage', and SMAP only sees the existing meltwater in its field of view. At the DY2 site (Figure 5c), LWA estimated by SMAP, and the EBM resemble more closely both in phase and magnitude (except the difference in timing of complete freeze up). This is reflected by nearly perfect correlation (r=0.98) and a small overall RMSD (4 mm) as shown.

SMAP LWA also closely aligns with the EBM at NSE site in magnitude and duration of liquid water presence (r = 0.98 and RMSD = 3 mm) although SMAP seemed to miss the late August small melt event (Figure 5e). The agreement however exhibits the greatest deficiencies at SDL site for this melt season (Figure 5f). Although the timing of the melt onset and late August secondary melt event matches precisely, the EBM reports overall a higher LWA and an extended summer melt duration at this location. This is manifested in the performance metrics shown by a relatively higher RMSD (24 mm) and comparatively lower correlation coefficient (0.77). The performance at SDM site is generally good (r = 0.92, and RMSD = 6 mm), except the EBM demonstrates a delayed refreezing than SMAP (Figure 5g).

It is pertinent to highlight that while *in situ* LWA at all these AWS were derived from the energy balance model forced by the pointwise measurements at the AWS locations, the SMAP retrievals estimated a spatially averaged LWA corresponding to the ~30 km effective resolution of the enhanced-resolution TB. Approximately, during the first half of the melt season, the LWA is primarily determined by meltwater generation in response to the net radiation flux at the surface. Whereas, roughly during the second half when the net radiation flux remains negative, refreezing becomes the dominant process. Hence, the model's representation of the surface melt infiltration, heat transfer, and other physical processes play a significant role, posing additional uncertainties. The AWS measurements used to run the model also add some inherent uncertainties. Therefore, assessing relative accuracies is not straightforward. Nevertheless, the general agreements between the model and SMAP retrieved LWA in magnitude and phase at these locations suggest that the spatial heterogeneity of melt processes is not acute in these areas.

398
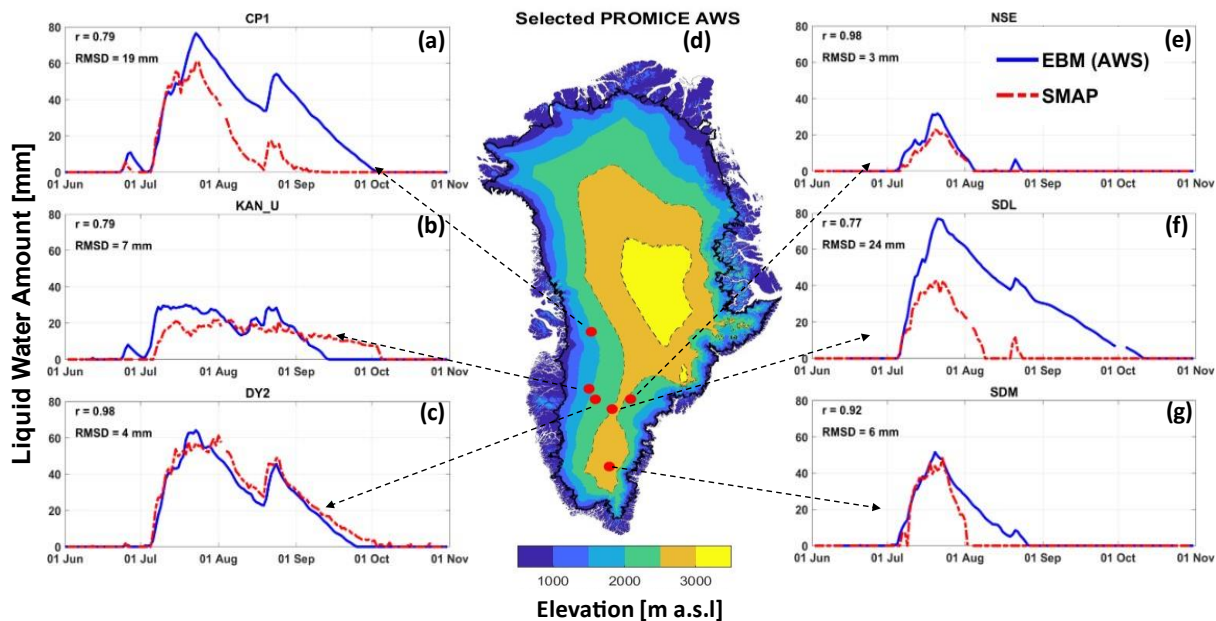
Figure 5: Comparison of the total daily liquid water amount retrieved from SMAP (red dashed lines labeled SMAP) and estimated by the EBM forced with *in situ* measurements (blue lines labeled EBM) at selected PROMICE and GC-Net AWS within the GrIS percolation area for Jun 1 – Oct 31, 2023. The locations of the AWSs are shown in the middle panel along with the ice sheet surface elevation (Howat et al., 2014).

3.1.2 Three Way Comparison: SMAP, EBM, and GEMB Model

We performed a pairwise comparison among SMAP, EBM, and GEMB models (Figure 6) for the 2021, 2022 and 2023 melt seasons (based on available meteorological data) at the 6 AWS locations. In detail performance metrics are documented in Table 1 (mean difference, STD, mean absolute difference, Pearson linear correlation coefficient, and RMSD) and Table 2 (melt onset, freeze up, duration of summer melt, maximum summer melt, and annual sum of daily LWA). Because of SMAP outage for 2022 summer, performance metrics in Table 1 only considered the operational part of SMAP. Table 2, however, excludes SMAP for 2022 melt season except the melt onset information as the other metrics were impacted by the outage.

At KAN_U site, the overall agreement between SMAP and the EBM was determined to be better (r > 0.75) than the agreement between SMAP and GEMB model (r < 0.55), for the 2021 and 2023 melt seasons (Figure 6a-6c). All the AWS data required to run the EBM for 2022 melt season were not available. GEMB used ERA5 data to gap fill this period, and SMAP LWA closely aligns with GEMB estimates for the first part of the summer season till the outage. However, GEMB model demonstrates earlier melt onset in 2021 and 2023 melt seasons compared to both SMAP and the EBM. SMAP estimated a maximum summer melt of 56 mm at this site in 2021 melt season, while both the EBM and GEMB model recorded maximum summer melt of 30 and 45 mm respectively in 2023 melt season. No pair shows consistent superiority at CP1 site
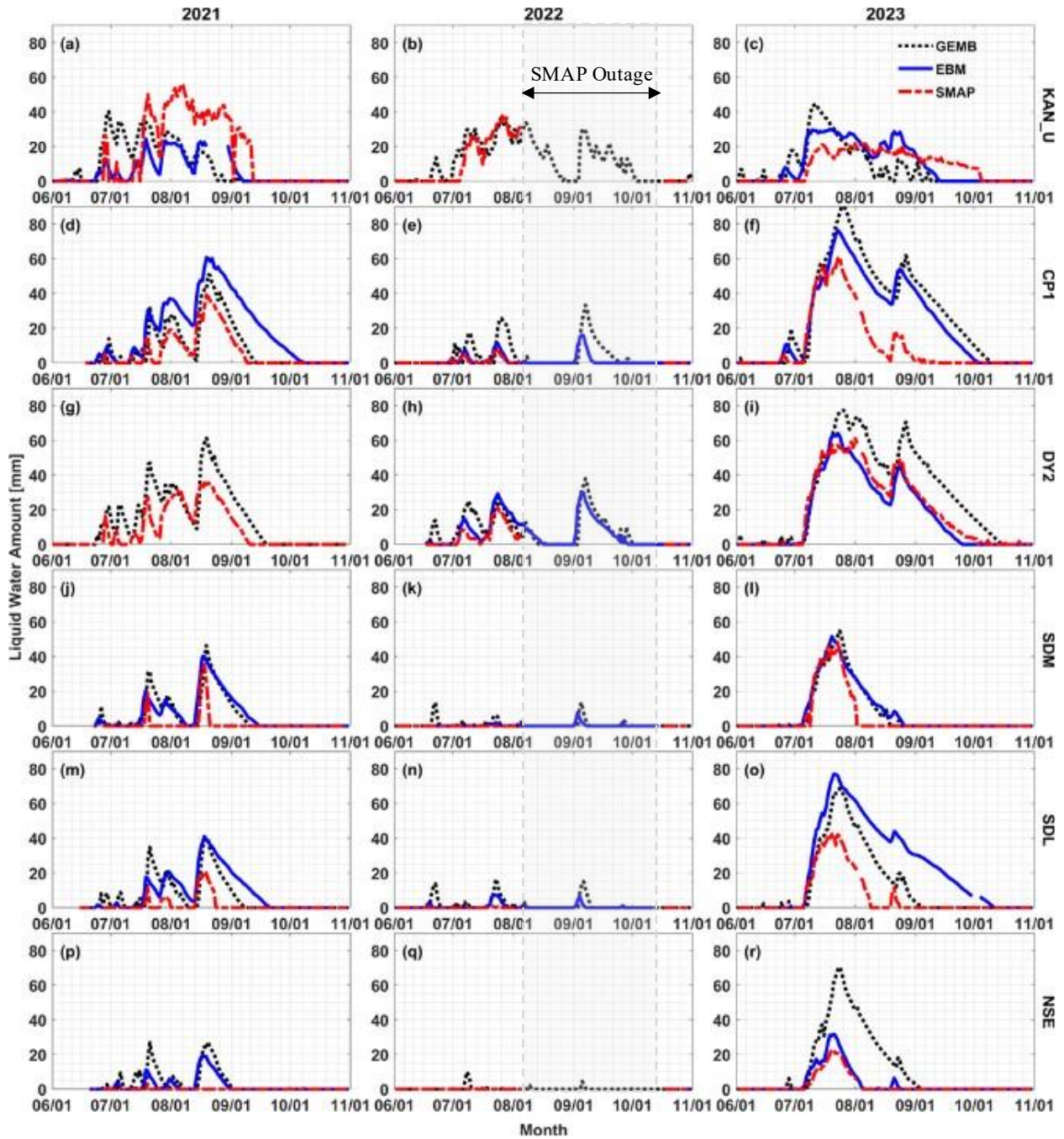
Figure 6: Comparison of the SMAP retrieved total daily liquid water amount (red dashed lines) with the estimated LWA from EBM (blue solid lines), and GEMB model (black dotted lines) at selected PROMICE and GC-Net AWS within the GrIS percolation area. SMAP data gap is depicted in shade for 2022 summer season, and EBM results were not included when AWS data were missing where GEMB used ERA5 forcing.

(Figure 6d-6f). SMAP LWA generally aligns closer with GEMB model LWA in 2021 melt season, and with the EBM in 2022 melt season, whereas in 2023 melt season, the EBM and GEMB model matches closer to each other than to SMAP. DY2 lacks AWS forcing during 2021 melt season. So, EBM result is missing for this melt season. Between SMAP and GEMB model, the later estimates overall more LWA (LWA$_{YS}$ 1196 mm vs 2101 mm). But there is a reasonable alignment between the peaks of the two LWA time series (Figure 6g). The overall RMSD was found to be 10.67 mm. For the other two melt seasons (Figure 6h-6i), SMAP and the EBM results show superior agreements (r > 0.96 and RMSD ~ 4 mm). GEMB model reports slightly higher LWA in 2023, both in magnitude and duration (4214 mm LWA$_{YS}$ compared to 2893 mm (SMAP) and 2608 mm (EBM) resulting in a higher overall RMSD (>12 mm) with the other two.

Table 1: Pairwise performance comparison among (a) SMAP, (b) EBM, and (c) GEMB models for 2021-2023 summer seasons (Jun 1 – Oct 31). Cells are left blank for missing either SMAP or AWS data.

AWS	Year	Mean Difference (mm)			Standard Deviation (STD) (mm)			Mean Absolute Difference (MAD) (mm)			Pearson Correlation Coefficient (r)			Root Mean Square Difference (RMSE) (mm)		
		a-b	a-c	b-c	a-b	a-c	b-c	|a-b|	|a-c|	|b-c|	a, b	a, c	b, c	a-b	a-c	b-c
KAN_U	2021	8.0	6.0	-3.9	12.72	17.78	9.24	8.82	12.53	5.44	0.85	0.43	0.65	14.99	18.73	10.02
	2022		-1.5			5.61			3.66			0.91			5.76	
	2023	-1.2	0.9	2.2	7.17	10.26	7.96	5.19	7.51	5.19	0.79	0.53	0.77	7.25	10.26	8.23
CP1	2021	-12.3	-3.3	8.7	10.68	6.41	9.31	12.35	4.43	9.22	0.88	0.90	0.87	16.30	7.21	12.72
	2022	-0.5	-3.1	-3.0	1.07	6.26	6.04	0.59	3.50	3.46	0.96	0.48	0.64	1.16	6.93	6.72
	2023	-12.3	-17.0	-4.8	14.57	17.88	5.94	12.79	17.66	5.81	0.79	0.77	0.98	19.00	24.62	7.62
DY2	2021		-6.0			8.86			6.62			0.86			10.67	
	2022	-2.8	-4.5	-1.2	3.45	5.74	4.97	2.85	4.75	3.01	0.96	0.73	0.84	4.42	7.26	5.09
	2023	2.2	-8.4	-10.5	3.72	9.68	10.70	2.96	9.49	10.81	0.98	0.94	0.93	4.30	12.78	14.97
SDM	2021	-5.3	-5.0	0.3	8.07	8.93	4.55	5.37	5.26	2.39	0.60	0.53	0.90	9.65	10.19	4.55
	2022	-0.2	-0.8	-0.5	0.45	2.29	2.23	0.23	0.79	0.81			0.37	0.50	2.41	2.28
	2023	-2.9	-2.2	0.5	5.62	5.69	2.81	3.09	2.75	1.35	0.92	0.92	0.98	6.33	6.09	2.85
SDL	2021	-6.7	-4.7	1.9	8.65	8.13	6.28	6.75	5.12	4.20	0.69	0.65	0.83	10.94	9.38	6.53
	2022	-0.7	-1.6	-0.9	1.75	3.53	2.78	0.73	1.58	1.12	0.69	0.35	0.62	1.88	3.84	2.91
	2023	-18.1	-6.1	11.1	16.40	10.53	9.88	18.13	6.53	11.19	0.77	0.89	0.92	24.37	12.16	14.81
NSE	2021	-2.1	-3.6	-1.5	4.46	6.74	4.08	2.08	3.61	2.19	0.15	0.16	0.80	4.90	7.62	4.33
	2022		-0.3			1.50			0.34						1.53	
	2023	-1.2	-9.4	-8.8	2.48	14.90	14.07	1.16	9.48	9.07	0.98	0.83	0.80	2.73	17.59	16.57

As per maximum summer melt and LWA$_{YS}$, SDL, SDM and NSE sites experienced the highest LWA in 2023 melt season compared to the other two melt seasons under consideration (Figure 6j-6r). SMAP did not record any LWA in any of these sites during 2022 melt season when EBM (except NSE where AWS data were not available), and GEMB models also reported the least LWA in three melt seasons (Figure 6k, 6n, and 6q). In 2021 melt season, SMAP estimated overall lower

LWA and shorter summer melt duration than that of EBM and GEMB models in these sites. But the agreements between EBM and GEMB models are in the same orders (see Table 1 and Table 2), with both exhibited delayed refreezing consistently compared to SMAP.

Table 2: Comparison of individual performances: (a) SMAP, (b) EBM, and (c) GEMB models. A threshold of 2 mm LWA was considered to avoid any spurious melt event. Comparisons were performed based on daily matchup dataset. Cells are left blank when significant data were missing during summer.

AWS	Year	Melt Onset (DOY)			Melt Freeze up (DOY)			Summer Melt Duration (days)			Maximum Summer LWA (mm)			Annual Sum of Daily LWA (mm-year)		
		SMAP	EBM	GEMB	SMAP	EBM	GEMB	SMAP	EBM	GEMB	SMAP	EBM	GEMB	SMAP	EBM	GEMB
KAN_U	2021	179	175	164	254	248	247	76	74	84	56	24	40	2212	736	1351
	2022	186		171			303			133			36			1709
	2023	188	176	154	277	254	251	90	79	98	22	30	45	1302	1504	1205
CP1	2021	179	175	177	251	277	254	73	103	78	39	61	51	842	2471	1288
	2022	181	181	182		252	272		72	91		16	33		175	589
	2023	175	176	154	246	273	280	72	98	127	61	76	91	1569	3458	4191
DY2	2021	179		175	251		260	73		86	35		61	1196		2101
	2022	185	185	171		270	273		86	103		30	38		838	1003
	2023	187	187	154	313	265	286	127	79	133	61	64	77	2893	2608	4214
SDM	2021	200	175	177	232	256	251	33	82	75	35	40	46	164	857	812
	2022		245	171		269	270		25	100		8	14		32	104
	2023	188	187	188	213	237	236	26	51	49	48	52	55	775	1202	1129
SDL	2021	200	185	177	235	261	249	36	77	73	21	41	40	195	1096	839
	2022		169	171		248	252		80	82		7	17		68	188
	2023	187	187	166	235	282	245	49	96	80	43	77	69	919	3383	1879
NSE	2021	201	185	180	201	241	243	1	57	64	3	19	27	5	271	469
	2022			188			249			62			10			37
	2023	188	187	178	214	234	244	27	48	67	23	32	70	338	508	1789

3.1.3 SMAP LWA Time Series

Figure 7 shows the SMAP retrieved LWA time series at the mentioned six AWS locations on the southwest and southeast sides of the GrIS percolation zone. The time series do not include results during 2019 and 2022 outage. As evidenced, the AWS sites in the southwest sites (Figure 7a-7c) experienced more average LWA and longer summer melt duration than the AWS sites in southeast sites (Figure 7d-7f). SDL, SDM, and NSE witnessed an insignificant LWA (<10 mm) during 2015 -

448 2020 melt seasons. However, it was found to be increasing in recent years (Figure 7d-7f). SMAP recorded the highest LWA
449 in 2023 melt season during 2015 - 2023 at all the AWS locations, except at KAN_U where 2021 marked the highest melt
450 season.

451

452
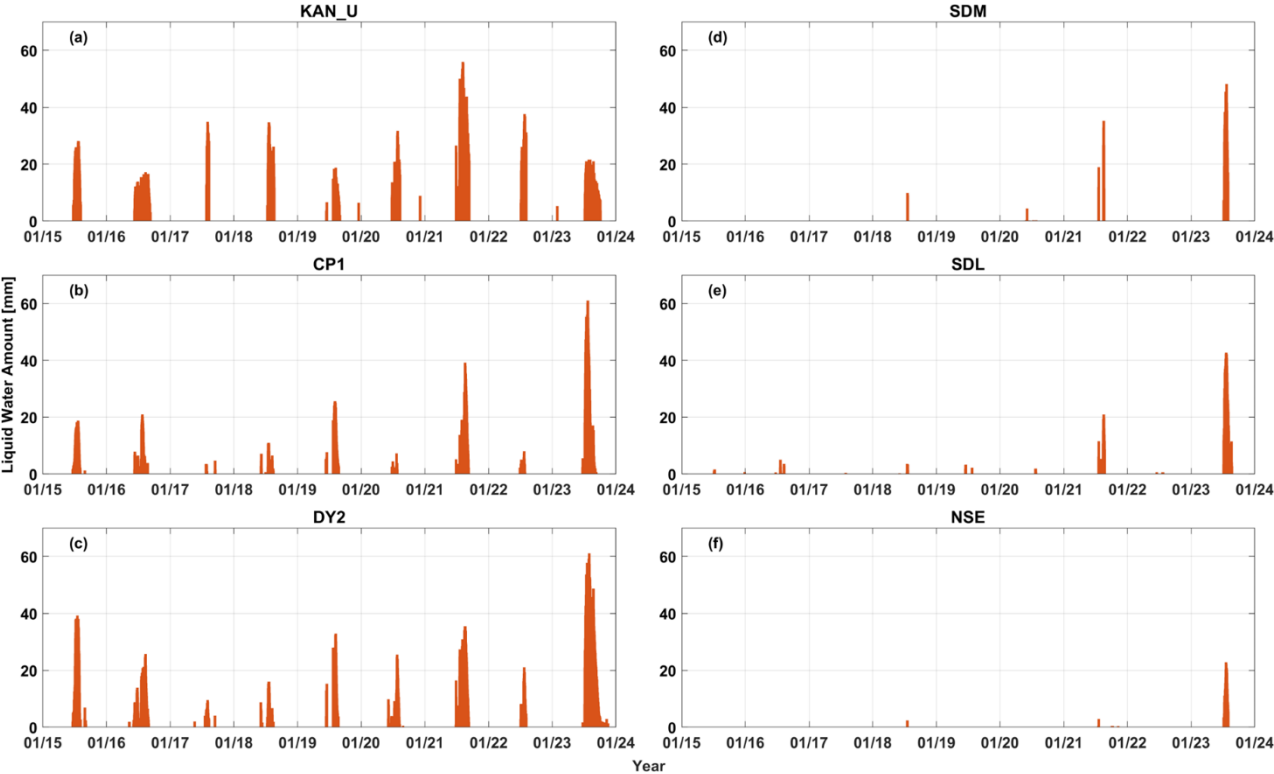
453 **Figure 7: SMAP retrieved LWA time series for 2015-2023 period at six selected PROMICE and GC-Net AWS within the GrIS**
454 **percolation area.**

455 **3.1.4 Spatial Variability**

456 Figure 8 illustrates the annual sum of daily LWA (LWA$_{YS}$) for 2015 – 2023. Here, we masked the area where melt is detected

457 by decreasing summer TBs (compared to winter reference). As mentioned in Sec. 2.2.3, current LWA quantification algorithm

458 applies to increasing TBs only. This excluded the melt flags in the ablation zone and upper accumulation zone as indicated by

459 grey shades in Figure 8. There were also some occasions when summer TB decreases below the winter threshold in the

460 percolation too. Those anomalies were probably caused by short lived melt events that refroze between SMAP passes and

461 impacted TBs. These anomalies are also masked and not included in the results. As depicted, SMAP captured the similar

462 spatial trends of LWA distribution across the percolation zone of GrIS as reported by previous studies (Van Den Broeke et al.,

463 2016; Houtz et al., 2021). In the time frame under consideration, 2023 melt season (Figure 8i) had the highest LWA$_{YS}$ (2634

464 mm on average for the percolation area) while 2017 (Figure 8c) had the lowest value (757 mm on average for the percolation

area). In 2015 (Figure 8a), the northern ice sheet exhibited a relatively high LWA$_{YS}$; similar intensity and extent were also recorded for 2023 (Figure 8i). Notably, the melt extended to upper elevations in the dry snow zone in 2021 and 2023. Unfortunately, SMAP outages in 2019 (Figure 8e) and 2022 (Figure 8h), lead to incomplete coverage for those years and lower LWA$_{YS}$. It is worthwhile to reiterate that the integrated LWA is a measure of the total seasonal LWA in the specified area.
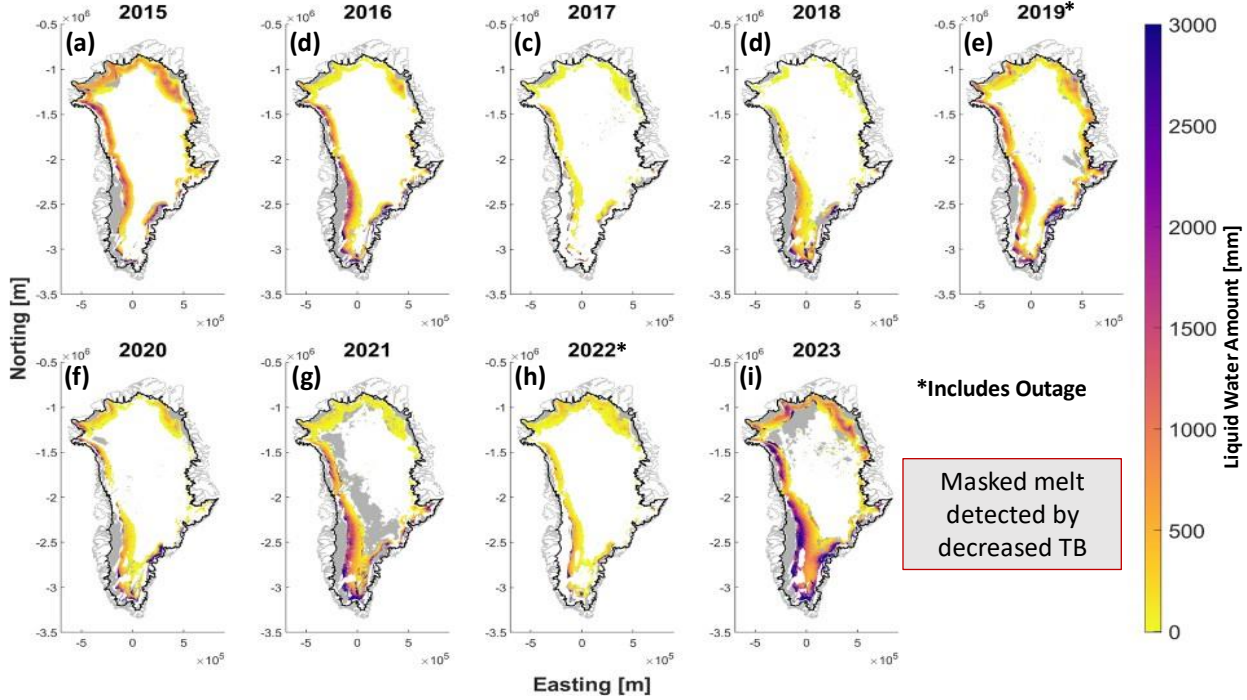
Figure 8: Total annual sum of SMAP daily LWA for 2015 - 2023. The black solid line represents GrIS edges, and the grey color masks inside the ice sheet indicate melt detections by decreasing TB, which were not quantified.

4 Discussion

The L-band radiometry has the unique advantage of receiving the emission from the deep layers of ice sheets, offering the opportunity to track meltwater from deeper layers. We have demonstrated its capability to estimate the seasonal LWA that generally agrees with two state-of-the-art ice sheet models, forced with independent *in situ* AWS measurements. The legitimacy of spatial and temporal variability shown in SMAP retrieval for the percolation area of the GrIS is promising.

There are some disagreements as well, but those do not necessarily indicate a deficiency of the SMAP retrievals since both the references are models with their own limitations. The differences between model results and SMAP retrievals are not systematic, so they are difficult to explain; but there is no evidence of a consistent bias. Nonetheless, some of the discrepancies between these estimations of LWA stem from the scale at which those datasets operate. The SMAP LWA was estimated from the TB measurements averaged over a large footprint and a short integration time. Further, rSIR enhanced-resolution data

products involve overlapping observations to produce the 3.125 km gridded data but still has an effective spatial resolution of ~30 km. Thus, it represents near-instantaneous vertically integrated LWA, averaged over the grid point, whereas the AWS data is the hourly average of 'point' measurements representative of the 0.1-1 km surrounding the station. The total LWA from AWS-forced data is the hourly-averaged, vertically integrated net water balance which is determined as the cumulative sum of hourly surface melt generation, refreezing, and drainage. The surface melt generation is driven by the net surface energy balance (net radiation and turbulent heat fluxes), which involves uncertainties (e.g., the surface albedo and roughness; errors in the meteorological inputs), while how the melt and heat are distributed in subsurface firn involves additional uncertainties, including sensitivity to initial conditions (e.g., the firn temperature and density profile; Samimi et al., 2020). These models transform surface meteorological information into an amount of surface melt relying on loosely constrained parameterizations (Covi et al., 2023). Eventually, the models' formulation for the meltwater infiltration is still poorly constrained (e.g. Vandecrux et al., 2020). Additionally, both the models we used (like other state-of-the-art firn models) are one dimensional – they only consider vertical movement of water and heat and do not account for horizontal advection. However, firn hydrological processes are complex and heterogeneous, and processes such as ice layer formation are intrinsically three-dimensional. What the models consider as 'drainage' (meltwater that moves out of the system) both vertically and horizontally could still be within the SMAP sensing depth and horizontal footprints. Hence, the comparison should be considered accordingly.

One important disagreement between SMAP and EBM LWA estimation, especially during the refreezing periods, is that EBM retained LWA for an extended period when SMAP showed complete refrozen condition (Figure 6). We used SUMup subsurface temperature measurements (Vandecrux et al., 2023b) to verify the cases for which SUMup data are available. One example is shown in Figure 9. It compares the model-estimated subsurface temperature (Figure 9a) corresponding to the 2021 LWA at CP1 (Figure 6d) to the *in situ* measured subsurface temperature (Figure 9b). It is evident that although the penetration depth of the model wetting front closely matches the observation, the measurement demonstrates a higher and faster refreezing compared to the model. The subsurface measurement shows a fully refrozen condition by early September (closely agreeing with what was revealed by SMAP, see Figure 6d). However, the model seems to retain the subsurface meltwater with a persistent wetting front even past the beginning of October, which seems unlikely. Speculating extra melt production due to possible error in the AWS surface forcing, and other surface processes in the EBM, we examined modelled subsurface temperature profile by reducing surface melt with different factors (<1). We also performed similar analysis with irreducible water content, thermal conductivity. In either case (not shown), we could not match the subsurface profile with measured profile within reasonable agreements. This incites questions regarding the model representation of meltwater infiltration, heat transfer, and refreezing.

The models do not include meltwater infiltration by finger flow (piping). Some recent studies have shown that this is an important mechanism for moving liquid water from the surface to deep depths (e.g., Vandecrux et al, 2020). The piping events are short-lived penetration and refreezing events. SMAP will measure the LWC in the piping event, even when it passes the wetting front, unless the water is refrozen before the SMAP measurement (as is the case with all short-lived melt events). The model would calculate a certain amount of meltwater based on the surface energy balance, and it would put all this water

into the wetting front layer. However, from the literature and as confirmed by the subsurface temperature measurements (Figure 9b), some fraction of this water would be partitioned into deep piping. The model only includes top-down migration of a wetting front. This may explain why there are discrepancies between the modelled subsurface temperature profile and the observed subsurface temperature profile in some cases. Indeed, the deep penetration events causing warming spikes beyond the wetting front distort the temperature profiles. Therefore, some differences between SMAP and the EBM and GEMB model could be attributed to this weakness in process representation in the model. But overall, these problems are multifaceted, and additional works are required to understand the basis for these discrepancies. Yet, to this day, there is no observational dataset that allows to evaluate directly the LWA retrieved from satellite observations or calculated by a snow and firn model.

Besides the coarser spatial resolution, SMAP algorithm has its own shortcomings. The emission model simulated TBs with a simplified view of the stratigraphy which lacks detailed representation of snow and firn microstructures. The model also neglected atmospheric contributions and assumed homogenous medium and smooth surface within each layer. Although these effects are not significant at L-band, a detailed characterization was not done. The detection algorithm follows a threshold-based technique that uses winter reference of the TB to detect melt events. As a result, it is capable quantifying the seasonal LWA only, not the LWA in perennial firn aquifers which stores a large quantity of saturated liquid water on the GrIS throughout the year (Montgomery et al., 2017;Miller et al., 2020b;Miller et al., 2020a). Miller et al., (2022a, b) developed empirical technique to map Greenland's perennial firn aquifers with SMAP L-band brightness temperature; however, without complementary observations of firn aquifers via other means such as radar sounding, while the detection itself is ambiguous, the quantification would be more challenging. Current algorithm also excluded areas where TB decreases during summer melt. Future work will be continued to overcome some of these limitations and refine the algorithm.

To extend the algorithm for GrIS-wide LWA quantification, the ablation zone presents a major challenge. Although SMAP can detect melt events in the ablation zone, the quantification is difficult for several reasons. The hydrological features of the ablation zone are markedly different from the percolation or upper accumulation zone. There are widespread networks of many supraglacial lakes and rivers, crevasses, and other complex heterogeneous factors, such as surface topography, dust deposition, slush saturation, etc. (Cooper and Smith, 2019; Poinar and C. Andrews, 2021; Smith et al., 2017). This generates an intricate radiometric response. The average LWA in ablation zone is also significantly higher limiting the L-band emission in the upper layer only. Houtz et al., (2019) used L-band observations from SMOS satellite to derive LWA at the Swiss Camp GC-Net AWS located in the ablation zone with a simplistic assumption of fixed (10 cm) wet layer thickness. More *in situ* observations are needed to characterize the spatial and temporal variability of LWA in the ablation zone.

545
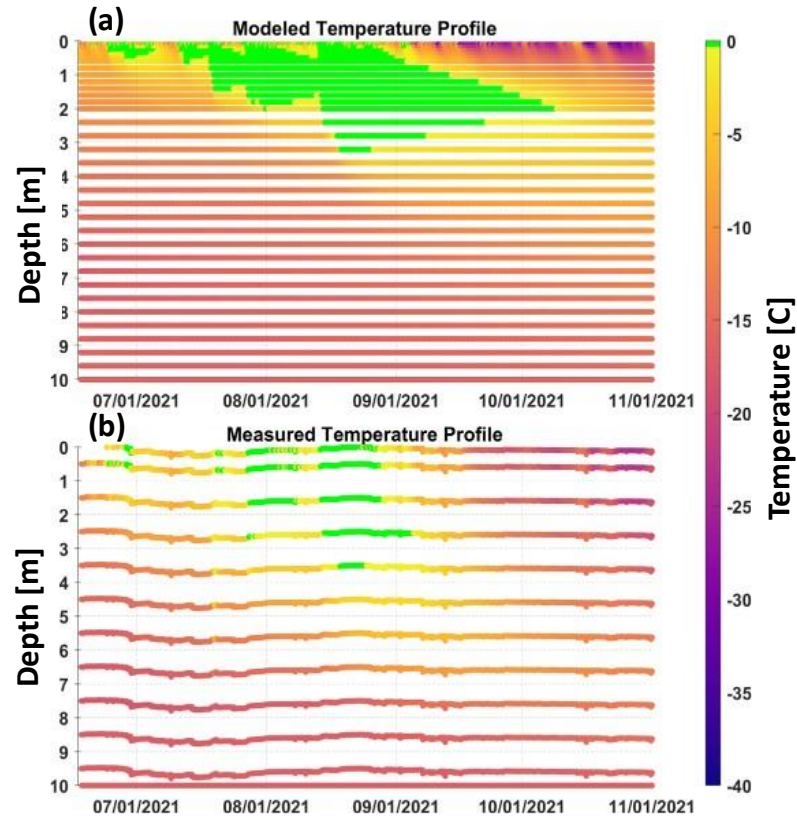
Figure 9: Modeled (a) and measured (b) subsurface temperatures corresponding to total LWA at CP1 site during 2021 melt season. The 0°C isotherm is highlighted by green color.

5 Conclusion

We have demonstrated quantification of the total surface and subsurface meltwater amount over the Greenland ice sheet using the L-band radiometric observations from the SMAP mission. The retrieval algorithm was described, and the validation results with six *in situ* weather station measurements and reanalysis data were provided. The comparison results were analysed, showing that the retrieval generally agrees with the AWS-driven LWA across the percolation zone. The model uncertainties in representing firn hydrological and thermal processes were explored, and the greatest differences involve the timescale for internal refreezing. The model results commonly predict a longer season for liquid water content in the snow and near-surface firn, i.e., delays in refreezing relative to the SMAP data. Limitations of the SAMP and model estimates LWA, and possible reasons for the discrepancies between them were discussed. Further work is required to understand the basis for these discrepancies and refine the algorithm. A detailed sensitivity analysis and uncertainty characterization of the LWA retrieval algorithm, including dielectric mixing models is required. The results demonstrate the potential for providing an observational dataset at time and space scales that will advance our understanding of ice sheet physical processes, helping to better project

Greenland's contribution to global sea level rise in response to climate change and variability. To create a longer time data product, integrating SMOS observations (2010 - present) with SMAP will be beneficial. The algorithm can easily be extended for LWA estimation in Antarctic Ice Sheet. ESA's upcoming CIMR mission (Copernicus Imaging Microwave Radiometer to be launched in 2029) will include coincident L (1.4 GHz) - Ka (36 GHz) channels for the first time (Colliander et al., 2024; Kilic et al., 2018), Future works should explore the added benefits of other complementary frequencies (6 GHz up to 36 GHz bands) in order to provide a possible depth profile of the LWC.

Data and code availability

SMAP Radiometer Twice-Daily rSIR-Enhanced EASE-Grid 2.0 Brightness Temperatures, Version 2 data products were provided by National Snow and Ice Data Center and are publicly available at https://nsidc.org/data/nsidc-0738/versions/2. The PROMICE hourly AWS measurements are available at https://doi.org/10.22008/FK2/IW73UU (How et al., 2022). The 2023 version of the SUMup subsurface temperature and density profiles are available at https://arcticdata.io/catalog/view/doi:10.18739/A2M61BR5M. SMAP and model LWA are available in a Zenodo repository at https://doi.org/10.5281/zenodo.13800047. The scripts used to perform the analysis for this study can be found at https://github.com/HossanAlamgir/SMAP_MWA_Retrieval_and_Validation_GrIS. MATLAB source code for glacier surface energy balance coupled with firn thermodynamic and hydrological modelling is available in PRISM Data: University of Calgary's Data Repository at https://doi.org/10.5683/SP2/WRWJAZ (Marshall, 2021).

Author contributions

AH and AC designed the study and the methodology. AH performed the formal analysis and visualization. NS run the GEMB model and provided the outputs. AH and AC prepared the first draft of the paper. All the authors discussed the results and reviewed the paper. AC supervised the project and managed funding.

Competing interests

The authors declare that they have no conflicts of interest.

Acknowledgements

This work was funded by the NASA Cryospheric Sciences Program; the work was conducted at the Jet Propulsion Laboratory, California Institute of Technology, under a contract with the National Aeronautics and Space Administration. BV

was supported by the Climate Change Initiative Fellowship from the European Space Agency. We gratefully acknowledge computational resources and support from the NASA Advanced Supercomputing Division. The Greenland maps were generated with the assistance of the Arctic Mapping Tools (Greene et al., 2017). The first author benefited from occasional use of ChatGPT (free version) for assistance with syntax and linguistic corrections during the preparation of this manuscript.

References

Abdalati, W. and Steffen, K.: Passive microwave-derived snow melt regions on the Greenland Ice Sheet, Geophys. Res. Lett., 22, 787–790, https://doi.org/10.1029/95GL00433, 1995.

Abdalati, W. and Steffen, K.: Snowmelt on the Greenland ice sheet as derived from passive microwave satellite data, J. Clim., 10, 165–175, https://doi.org/10.1175/1520-0442(1997)010<0165:SOTGIS>2.0.CO;2, 1997.

Abdalati, W. and Steffen, K.: Greenland Ice Sheet melt extent: 1979–1999, J. Geophys. Res. Atmos., 106, 33983–33988, https://doi.org/https://doi.org/10.1029/2001JD900181, 2001.

Ashcraft, I. and Long, D.: Comparison of methods for melt detection over greenland using active and passive Microwave measurements, Int. J. Remote Sens., 27, 2469–2488, https://doi.org/10.1080/01431160500534465, 2006.

Brodzik, M. J., Long, D. G., and Hardman, M. A.: SMAP Twice-Daily rSIR-Enhanced, 1–51, 2021.

Van Den Broeke, M. R., Enderlin, E. M., Howat, I. M., Kuipers Munneke, P., Noël, B. P. Y., Jan Van De Berg, W., Van Meijgaard, E., and Wouters, B.: On the recent contribution of the Greenland ice sheet to sea level change, Cryosphere, 10, 1933–1946, https://doi.org/10.5194/tc-10-1933-2016, 2016.

Calonne, N., Milliancourt, L., Burr, A., Philip, A., Martin, C. L., Flin, F., and Geindreau, C.: Thermal Conductivity of Snow, Firn, and Porous Ice From 3-D Image-Based Computations, Geophys. Res. Lett., 46, 13079–13089, https://doi.org/10.1029/2019GL085228, 2019.

Chaubell, J., Yueh, S., Peng, J., Dunbar, S., Chan, S., Chen, F., Piepmeier, J., Bindlish, R., Entekhabi, D., and O'Neill, P.: Soil Moisture Active Passive (SMAP) Algorithm Theoretical Basis Document: SMAP L1(B/C) Enhanced Radiometer Brightness Temperature Data Product, 1, 1–32, 2018.

Chaubell, M. J., Chan, S., Dunbar, R. S., Peng, J., and Yueh, S.: SMAP Enhanced L1C Radiometer Half-Orbit 9 km EASE-Grid Brightness Temperatures, Version 1., 2020.

Citterio, M. and Ahlstrøm, A. P.: Brief communication the aerophotogrammetric map of Greenland ice masses, Cryosphere, 7, 445–449, https://doi.org/10.5194/tc-7-445-2013, 2013.

Colbeck, S. C.: Theory of Metamorphism of Wet Snow., US Army Corps Eng Cold Reg Res Eng Lab Res Rep, 88, 5475–5482, 1973.

Colbeck, S. C.: The capillary effects on water percolation in homogeneous snow, J. Glaciol., 13, 85–97, https://doi.org/10.3189/s002214300002339x, 1974.

Coléou, C. and Lesaffre, B.: Irreducible water saturation in snow: experimental results in a cold laboratory, Ann. Glaciol., 26,

64–68, https://doi.org/10.3189/1998aog26-1-64-68, 1998.

Colliander, A., Mousavi, M., Misra, S., Brown, S., Kimball, J. S., Miller, J., Johnson, J., and Burgin, M.: Ice Sheet Melt Water Profile Mapping Using Multi-Frequency Microwave Radiometry, Int. Geosci. Remote Sens. Symp., 2022-July, 4178–4181, https://doi.org/10.1109/IGARSS46834.2022.9883717, 2022a.

Colliander, A., Mousavi, M., Marshall, S., Samimi, S., Kimball, J. S., Miller, J. Z., Johnson, J., and Burgin, M.: Ice Sheet Surface and Subsurface Melt Water Discrimination Using Multi-Frequency Microwave Radiometry, Geophys. Res. Lett., 49, https://doi.org/10.1029/2021GL096599, 2022b.

Colliander, A., Mousavi, M., Kimball, J. S., Miller, J. Z., and Burgin, M.: Spatial and temporal differences in surface and subsurface meltwater distribution over Greenland ice sheet using multi-frequency passive microwave observations, Remote Sens. Environ., 295, 113705, https://doi.org/10.1016/j.rse.2023.113705, 2023.

Colliander, A., Hossan, A., Harper, J., Vandecrux, B., Miller, J., Marshall, S., and Donlon, C.: Towards Ice Sheet and Ice Shelf Meltwater Profile Retrieval from Copernicus Imaging Microwave Radiometer (CIMR), 4–5, 2024.

Colosio, P., Tedesco, M., Ranzi, R., and Fettweis, X.: Surface melting over the Greenland ice sheet derived from enhanced resolution passive microwave brightness temperatures (1979-2019), Cryosphere, 15, 2623–2646, https://doi.org/10.5194/tc-15-2623-2021, 2021.

Cooper, M. G. and Smith, L. C.: Satellite remote sensing of the Greenland Ice Sheet Ablation Zone: A review, Remote Sens., 11, 17–21, https://doi.org/10.3390/rs11202405, 2019.

Covi, F., Hock, R., and Reijmer, C. H.: Challenges in modeling the energy balance and melt in the percolation zone of the Greenland ice sheet, J. Glaciol., 69, 164–178, https://doi.org/10.1017/jog.2022.54, 2023.

Culberg, R., Schroeder, D. M., and Chu, W.: Extreme melt season ice layers reduce firn permeability across Greenland, Nat. Commun., 12, 1–9, https://doi.org/10.1038/s41467-021-22656-5, 2021.

Ebrahimi, S. and Marshall, S. J.: Surface energy balance sensitivity to meteorological variability on Haig Glacier, Canadian Rocky Mountains, Cryosphere, 10, 2799–2819, https://doi.org/10.5194/tc-10-2799-2016, 2016.

Elachi, C., and Van Zyl, J. J.: Introduction to the Physics and Techniques of Remote Sensing, John Wiley & Sons, 159–189 pp., https://doi.org/https://doi.org/10.1002/9781119523048.ch5, 2021.

Entekhabi, D., Njoku, E. G., O'Neill, P. E., Kellogg, K. H., Crow, W. T., Edelstein, W. N., Entin, J. K., Goodman, S. D., Jackson, T. J., Johnson, J., Kimball, J., Piepmeier, J. R., Koster, R. D., Martin, N., McDonald, K. C., Moghaddam, M., Moran, S., Reichle, R., Shi, J. C., Spencer, M. W., Thurman, S. W., Tsang, L., and Van Zyl, J.: The soil moisture active passive (SMAP) mission, Proc. IEEE, 98, 704–716, https://doi.org/10.1109/JPROC.2010.2043918, 2010.

Fausto, R. S., Van As, D., Mankoff, K. D., Vandecrux, B., Citterio, M., Ahlstrøm, A. P., Andersen, S. B., Colgan, W., Karlsson, N. B., Kjeldsen, K. K., Korsgaard, N. J., Larsen, S. H., Nielsen, S., Pedersen, A., Shields, C. L., Solgaard, A. M., and Box, J. E.: Programme for Monitoring of the Greenland Ice Sheet (PROMICE) automatic weather station data, Earth Syst. Sci. Data, 13, 3819–3845, https://doi.org/10.5194/essd-13-3819-2021, 2021.

Fettweis, X., van Ypersele, J. P., Gallée, H., Lefebre, F., and Lefebvre, W.: The 1979-2005 Greenland ice sheet melt extent

from passive microwave data using an improved version of the melt retrieval XPGR algorithm, Geophys. Res. Lett., 34, https://doi.org/10.1029/2006GL028787, 2007.

Fettweis, X., Tedesco, M., Van Den Broeke, M., and Ettema, J.: Melting trends over the Greenland ice sheet (1958-2009) from spaceborne microwave data and regional climate models, Cryosphere, 5, 359–375, https://doi.org/10.5194/tc-5-359-2011, 2011.

Fettweis, X., Hofer, S., Krebs-Kanzow, U., Amory, C., Aoki, T., Berends, C. J., Born, A., Box, J. E., Delhasse, A., Fujita, K., Gierz, P., Goelzer, H., Hanna, E., Hashimoto, A., Huybrechts, P., Kapsch, M. L., King, M. D., Kittel, C., Lang, C., Langen, P. L., Lenaerts, J. T. M., Liston, G. E., Lohmann, G., Mernild, S. H., Mikolajewicz, U., Modali, K., Mottram, R. H., Niwano, M., Noël, B., Ryan, J. C., Smith, A., Streffing, J., Tedesco, M., Jan Van De Berg, W., Van Den Broeke, M., Van De Wal, R. S. W., Van Kampenhout, L., Wilton, D., Wouters, B., Ziemen, F., and Zolles, T.: GrSMBMIP: Intercomparison of the modelled 1980-2012 surface mass balance over the Greenland Ice Sheet, Cryosphere, 14, 3935–3958, https://doi.org/10.5194/tc-14-3935-2020, 2020.

Gardner, A. S., Schlegel, N. J., and Larour, E.: Glacier Energy and Mass Balance (GEMB): A model of firn processes for cryosphere research, Geosci. Model Dev., 16, 2277–2302, https://doi.org/10.5194/gmd-16-2277-2023, 2023.

Greene, C. A., Gwyther, D. E., and Blankenship, D. D.: Antarctic Mapping Tools for MATLAB, Comput. Geosci., 104, 151–157, https://doi.org/10.1016/j.cageo.2016.08.003, 2017.

Greene, C. A., Gardner, A. S., Wood, M., and Cuzzone, J. K.: Ubiquitous acceleration in Greenland Ice Sheet calving from 1985 to 2022, 625, https://doi.org/10.1038/s41586-023-06863-2, 2024.

Hall, D. K., Nghiem, S. V., Schaaf, C. B., DiGirolamo, N. E., and Neumann, G.: Evaluation of surface and near-surface melt characteristics on the Greenland ice sheet using MODIS and QuikSCAT data, J. Geophys. Res. Earth Surf., 114, 1–13, https://doi.org/10.1029/2009JF001287, 2009.

Hallikainen, M. T., Ulaby, F. T., and Abdelrazik, M.: Dielectric Properties of Snow in the 3 To 37 Ghz Range., IEEE Trans. Antennas Propag., AP-34, 1329–1340, https://doi.org/10.1109/tap.1986.1143757, 1986.

Harper, J., Humphrey, N., Pfeffer, W. T., Brown, J., and Fettweis, X.: Greenland ice-sheet contribution to sea-level rise buffered by meltwater storage in firn, Nature, 491, 240–243, https://doi.org/10.1038/nature11566, 2012.

Heilig, A., Eisen, O., MacFerrin, M., Tedesco, M., and Fettweis, X.: Seasonal monitoring of melt and accumulation within the deep percolation zone of the Greenland Ice Sheet and comparison with simulations of regional climate modeling, Cryosphere, 12, 1851–1866, https://doi.org/10.5194/tc-12-1851-2018, 2018.

Herron MM and Langway CC: Firn densification: an empirical model. Journal of Glaciology 25(93), 373–385. doi:, 25, 1980.

Hersbach, H., Bell, B., Berrisford, P., Hirahara, S., Horányi, A., Muñoz-Sabater, J., Nicolas, J., Peubey, C., Radu, R., Schepers, D., Simmons, A., Soci, C., Abdalla, S., Abellan, X., Balsamo, G., Bechtold, P., Biavati, G., Bidlot, J., Bonavita, M., De Chiara, G., Dahlgren, P., Dee, D., Diamantakis, M., Dragani, R., Flemming, J., Forbes, R., Fuentes, M., Geer, A., Haimberger, L., Healy, S., Hogan, R. J., Hólm, E., Janisková, M., Keeley, S., Laloyaux, P., Lopez, P., Lupu, C., Radnoti, G., de Rosnay, P., Rozum, I., Vamborg, F., Villaume, S., and Thépaut, J. N.: The ERA5 global reanalysis, Q. J. R. Meteorol. Soc., 146, 1999–

2049, https://doi.org/10.1002/qj.3803, 2020.

Hoffman, M. J., Catania, G. A., Neumann, T. A., Andrews, L. C., and Rumrill, J. A.: Links between acceleration, melting, and supraglacial lake drainage of the western Greenland Ice Sheet, J. Geophys. Res. Earth Surf., 116, 1–16, https://doi.org/10.1029/2010JF001934, 2011.

Houtz, D., Naderpour, R., Schwank, M., and Steffen, K.: Snow wetness and density retrieved from L-band satellite radiometer observations over a site in the West Greenland ablation zone, Remote Sens. Environ., 235, 111361, https://doi.org/10.1016/j.rse.2019.111361, 2019.

Houtz, D., Mätzler, C., Naderpour, R., Schwank, M., and Steffen, K.: Quantifying Surface Melt and Liquid Water on the Greenland Ice Sheet using L-band Radiometry, Remote Sens. Environ., 256, https://doi.org/10.1016/j.rse.2021.112341, 2021.

How, P., Abermann, J., Ahlstrøm, A. P., Andersen, S. B., Box, J. E., Citterio, M., Colgan, W. T., R.S., F., Karlsson, N. B., Jakobsen, J., Langley, K., Larsen, S. H., Lund, M. C., Mankoff, K. D., Pedersen, A. Ø., Rutishauser, A., Shield, C. L., Solgaard, A. M., van As, D., Vandecrux, B., and Wright, P. J.: PROMICE and GC-Net automated weather station data in Greenland, https://doi.org/doi:10.22008/FK2/IW73UU, 2022.

Jay Zwally, H.: Microwave Emissivity and Accumulation Rate of Polar Firn, J. Glaciol., 18, 195–215, https://doi.org/10.3189/s0022143000021304, 1977.

Jezek, K. C., Johnson, J. T., Tan, S., Tsang, L., Andrews, M. J., Brogioni, M., MacElloni, G., Durand, M., Chen, C. C., Belgiovane, D. J., Duan, Y., Yardim, C., Li, H., Bringer, A., Leuski, V., and Aksoy, M.: 500-2000-MHz Brightness Temperature Spectra of the Northwestern Greenland Ice Sheet, IEEE Trans. Geosci. Remote Sens., 56, 1485–1496, https://doi.org/10.1109/TGRS.2017.2764381, 2018.

Jin, Y.-Q.: Electromagnetic Scattering Modelling for Quantitative Remote Sensing, WORLD SCIENTIFIC, 348 pp., https://doi.org/doi:10.1142/2253, 1994.

Jin, Y.: Radiative transfer theory at satellite-borne SSM/I channels and remote sensing data analysis, Sci. China, Ser. E Technol. Sci., 40, 644–652, https://doi.org/10.1007/bf02916850, 1997.

Jullien, N., Tedstone, A. J., Machguth, H., Karlsson, N. B., and Helm, V.: Greenland Ice Sheet Ice Slab Expansion and Thickening, Geophys. Res. Lett., 50, 1–9, https://doi.org/10.1029/2022GL100911, 2023.

Khan, S. A., Aschwanden, A., BjØrk, A. A., Wahr, J., Kjeldsen, K. K., and Kjaær, K. H.: Greenland ice sheet mass balance: A review, Reports Prog. Phys., 78, https://doi.org/10.1088/0034-4885/78/4/046801, 2015.

Khan, S. A., Bamber, J. L., Rignot, E., Helm, V., Aschwanden, A., Holland, D. M., van den Broeke, M., King, M., Noël, B., Truffer, M., Humbert, A., Colgan, W., Vijay, S., and Kuipers Munneke, P.: Greenland Mass Trends From Airborne and Satellite Altimetry During 2011–2020, J. Geophys. Res. Earth Surf., 127, 1–20, https://doi.org/10.1029/2021JF006505, 2022.

Kilic, L., Prigent, C., Aires, F., Boutin, J., Heygster, G., Tonboe, R. T., Roquet, H., Jimenez, C., and Donlon, C.: Expected Performances of the Copernicus Imaging Microwave Radiometer (CIMR) for an All-Weather and High Spatial Resolution Estimation of Ocean and Sea Ice Parameters, J. Geophys. Res. Ocean., 123, 7564–7580, https://doi.org/10.1029/2018JC014408, 2018.

Long, D. G., Brodzik, M. J., and Hardman, M. A.: Enhanced-Resolution SMAP Brightness Temperature Image Products, IEEE Trans. Geosci. Remote Sens., 57, 4151–4163, https://doi.org/10.1109/TGRS.2018.2889427, 2019.

Long, D. G., Brodzik, M. J., and Hardman, M.: Evaluating the effective resolution of enhanced resolution SMAP brightness temperature image products, Front. Remote Sens., 4, 1–10, https://doi.org/10.3389/frsen.2023.1073765, 2023.

MacFerrin, M., Machguth, H., As, D. van, Charalampidis, C., Stevens, C. M., Heilig, A., Vandecrux, B., Langen, P. L., Mottram, R., Fettweis, X., Broeke, M. R. va. den, Pfeffer, W. T., Moussavi, M. S., and Abdalati, W.: Rapid expansion of Greenland's low-permeability ice slabs, Nature, 573, 403–407, https://doi.org/10.1038/s41586-019-1550-3, 2019.

Machguth, H., Macferrin, M., Van As, D., Box, J. E., Charalampidis, C., Colgan, W., Fausto, R. S., Meijer, H. A. J., Mosley-Thompson, E., and Van De Wal, R. S. W.: Greenland meltwater storage in firn limited by near-surface ice formation, Nat. Clim. Chang., 6, 390–393, https://doi.org/10.1038/nclimate2899, 2016.

Marshall, S. J.: MATLAB code for firn thermodynamic and hydrological modeling, 2021.

Medley, B., Neumann, T. A., Zwally, H. J., Smith, B. E., and Stevens, C. M.: Simulations of firn processes over the Greenland and Antarctic ice sheets: 1980-2021, Cryosphere, 16, 3971–4011, https://doi.org/10.5194/tc-16-3971-2022, 2022.

Meyer, C. R. and Hewitt, I. J.: A continuum model for meltwater flow through compacting snow, Cryosphere, 11, 2799–2813, https://doi.org/10.5194/tc-11-2799-2017, 2017.

Mikkelsen, A. B., Hubbard, A., Macferrin, M., Eric Box, J., Doyle, S. H., Fitzpatrick, A., Hasholt, B., Bailey, H. L., Lindbäck, K., and Pettersson, R.: Extraordinary runoff from the Greenland ice sheet in 2012 amplified by hypsometry and depleted firn retention, Cryosphere, 10, 1147–1159, https://doi.org/10.5194/tc-10-1147-2016, 2016.

Miller, J. Z., Long, D. G., Jezek, K. C., Johnson, J. T., Brodzik, M. J., Shuman, C. A., Koenig, L. S., and Scambos, T. A.: Brief communication: Mapping Greenland's perennial firn aquifers using enhanced-resolution L-band brightness temperature image time series, Cryosphere, 14, 2809–2817, https://doi.org/10.5194/tc-14-2809-2020, 2020a.

Miller, J. Z., Culberg, R., Long, D. G., Shuman, C. A., Schroeder, D. M., and Brodzik, M. J.: An empirical algorithm to map perennial firn aquifers and ice slabs within the Greenland Ice Sheet using satellite L-band microwave radiometry, Cryosphere, 16, 103–125, https://doi.org/10.5194/tc-16-103-2022, 2022a.

Miller, J. Z., Long, D. G., Shuman, C. A., Culberg, R., Hardman, M., and Brodzik, M. J.: Mapping Firn Saturation Over Greenland Using NASA's Soil Moisture Active Passive Satellite, IEEE J. Sel. Top. Appl. Earth Obs. Remote Sens., 15, 3714–3729, https://doi.org/10.1109/JSTARS.2022.3154968, 2022b.

Miller, O., Solomon, D. K., Miège, C., Koenig, L., Forster, R., Schmerr, N., Ligtenberg, S. R. M., Legchenko, A., Voss, C. I., Montgomery, L., and McConnell, J. R.: Hydrology of a Perennial Firn Aquifer in Southeast Greenland: An Overview Driven by Field Data, Water Resour. Res., 56, https://doi.org/10.1029/2019WR026348, 2020b.

Montgomery, L. N., Schmerr, N., Burdick, S., Forster, R. R., Koenig, L., Legchenko, A., Ligtenberg, S., Miège, C., Miller, O. L., and Solomon, D. K.: Investigation of firn aquifer structure in southeastern Greenland using active source seismology, Front. Earth Sci., 5, 1–12, https://doi.org/10.3389/feart.2017.00010, 2017.

Mote, T. L.: Greenland surface melt trends 1973-2007: Evidence of a large increase in 2007, Geophys. Res. Lett., 34, 1–5,

755   https://doi.org/10.1029/2007GL031976, 2007.

756   Mote, T. L. and Anderson, M. R.: Variations in snowpack melt on the Greenland ice sheet based on passive-microwave

757   measurements, J. Glaciol., 41, 51–60, https://doi.org/10.1017/S0022143000017755, 1995.

758   Mouginot, J., Rignot, E., Bjørk, A. A., van den Broeke, M., Millan, R., Morlighem, M., Noël, B., Scheuchl, B., and Wood,

759   M.: Forty-six years of Greenland Ice Sheet mass balance from 1972 to 2018, Proc. Natl. Acad. Sci. U. S. A., 116, 9239–9244,

760   https://doi.org/10.1073/pnas.1904242116, 2019.

761   Mousavi, M., Colliander, A., Miller, J. Z., Entekhabi, D., Johnson, J. T., Shuman, C. A., Kimball, J. S., and Courville, Z. R.:

762   Evaluation of Surface Melt on the Greenland Ice Sheet Using SMAP L-Band Microwave Radiometry, IEEE J. Sel. Top. Appl.

763   Earth Obs. Remote Sens., 14, 11439–11449, https://doi.org/10.1109/JSTARS.2021.3124229, 2021.

764   Mousavi, M., Colliander, A., Miller, J., and Kimball, J. S.: A Novel Approach to Map the Intensity of Surface Melting on the

765   Antarctica Ice Sheet Using SMAP L-Band Microwave Radiometry, IEEE J. Sel. Top. Appl. Earth Obs. Remote Sens., 15,

766   1724–1743, https://doi.org/10.1109/JSTARS.2022.3147430, 2022.

767   Naderpour, R., Houtz, D., and Schwank, M.: Snow wetness retrieved from close-range L-band radiometry in the western

768   Greenland ablation zone, J. Glaciol., 67, 27–38, https://doi.org/10.1017/jog.2020.79, 2021.

769   Nghiem, S. V., Steffen, K., Kwok, R., and Tsai, W. Y.: Detection of snowmelt regions on the Greenland ice sheet using diurnal

770   backscatter change, J. Glaciol., 47, 539–547, https://doi.org/10.3189/172756501781831738, 2001.

771   Noël, B., Jan Van De Berg, W., MacHguth, H., Lhermitte, S., Howat, I., Fettweis, X., and Van Den Broeke, M. R.: A daily, 1

772   km resolution data set of downscaled Greenland ice sheet surface mass balance (1958-2015), Cryosphere, 10, 2361–2377,

773   https://doi.org/10.5194/tc-10-2361-2016, 2016.

774   Otosaka, I. N., Shepherd, A., Ivins, E. R., Schlegel, N. J., Amory, C., Van Den Broeke, M. R., Horwath, M., Joughin, I., King,

775   M. D., Krinner, G., Nowicki, S., Payne, A. J., Rignot, E., Scambos, T., Simon, K. M., Smith, B. E., Sørensen, L. S., Velicogna,

776   I., Whitehouse, P. L., Geruo, A., Agosta, C., Ahlstrøm, A. P., Blazquez, A., Colgan, W., Engdahl, M. E., Fettweis, X., Forsberg,

777   R., Gallée, H., Gardner, A., Gilbert, L., Gourmelen, N., Groh, A., Gunter, B. C., Harig, C., Helm, V., Khan, S. A., Kittel, C.,

778   Konrad, H., Langen, P. L., Lecavalier, B. S., Liang, C. C., Loomis, B. D., McMillan, M., Melini, D., Mernild, S. H., Mottram,

779   R., Mouginot, J., Nilsson, J., Noël, B., Pattle, M. E., Peltier, W. R., Pie, N., Roca, M., Sasgen, I., Save, H. V., Seo, K. W.,

780   Scheuchl, B., Schrama, E. J. O., Schröder, L., Simonsen, S. B., Slater, T., Spada, G., Sutterley, T. C., Vishwakarma, B. D.,

781   Van Wessem, J. M., Wiese, D., Van Der Wal, W., and Wouters, B.: Mass balance of the Greenland and Antarctic ice sheets

782   from 1992 to 2020, Earth Syst. Sci. Data, 15, 1597–1616, https://doi.org/10.5194/essd-15-1597-2023, 2023.

783   Paolo, F. S., Gardner, A. S., Greene, C. A., Nilsson, J., Schodlok, M. P., Schlegel, N. J., and Fricker, H. A.: Widespread

784   slowdown in thinning rates of West Antarctic ice shelves, Cryosphere, 17, 3409–3433, https://doi.org/10.5194/tc-17-3409-

785   2023, 2023.

786   Picard, G., Brucker, L., Roy, A., Dupont, F., Fily, M., Royer, A., and Harlow, C.: Simulation of the microwave emission of

787   multi-layered snowpacks using the Dense Media Radiative transfer theory: the DMRT-ML model, Geosci. Model Dev., 6,

788   1061–1078, https://doi.org/10.5194/gmd-6-1061-2013, 2013.

789 Picard, G., Leduc-Leballeur, M., Banwell, A. F., Brucker, L., and Macelloni, G.: The sensitivity of satellite microwave

790 observations to liquid water in the Antarctic snowpack, Cryosphere, 16, 5061–5083, https://doi.org/10.5194/tc-16-5061-2022,

791 2022.

792 Piepmeier, J. R., Focardi, P., Horgan, K. A., Knuble, J., Ehsan, N., Lucey, J., Brambora, C., Brown, P. R., Hoffman, P. J.,

793 French, R. T., Mikhaylov, R. L., Kwack, E. Y., Slimko, E. M., Dawson, D. E., Hudson, D., Peng, J., Mohammed, P. N., De

794 Amici, G., Freedman, A. P., Medeiros, J., Sacks, F., Estep, R., Spencer, M. W., Chen, C. W., Wheeler, K. B., Edelstein, W.

795 N., O'Neill, P. E., and Njoku, E. G.: SMAP L-Band Microwave Radiometer: Instrument Design and First Year on Orbit, IEEE

796 Trans. Geosci. Remote Sens., 55, 1954–1966, https://doi.org/10.1109/TGRS.2016.2631978, 2017.

797 Poinar, K. and C. Andrews, L.: Challenges in predicting Greenland supraglacial lake drainages at the regional scale,

798 Cryosphere, 15, 1455–1483, https://doi.org/10.5194/tc-15-1455-2021, 2021.

799 Samimi, S., Marshall, S. J., and MacFerrin, M.: Meltwater Penetration Through Temperate Ice Layers in the Percolation Zone

800 at DYE-2, Greenland Ice Sheet, Geophys. Res. Lett., 47, 1–9, https://doi.org/10.1029/2020GL089211, 2020.

801 Samimi, S., Marshall, S. J., Vandecrux, B., and MacFerrin, M.: Time-Domain Reflectometry Measurements and Modeling of

802 Firn Meltwater Infiltration at DYE-2, Greenland, J. Geophys. Res. Earth Surf., 126, https://doi.org/10.1029/2021JF006295,

803 2021.

804 Schoof, C.: Ice-sheet acceleration driven by melt supply variability, Nature, 468, 803–806,

805 https://doi.org/10.1038/nature09618, 2010.

806 Schwank, M. and Naderpour, R.: Snow density and ground permittivity retrieved from L-band radiometry: Melting effects,

807 Remote Sens., 10, 1–26, https://doi.org/10.3390/rs10020354, 2018.

808 Schwank, M., Rautiainen, K., Mätzler, C., Stähli, M., Lemmetyinen, J., Pulliainen, J., Vehviläinen, J., Kontu, A., Ikonen, J.,

809 Ménard, C. B., Drusch, M., Wiesmann, A., and Wegmüller, U.: Model for microwave emission of a snow-covered ground

810 with focus on L band, Remote Sens. Environ., 154, 180–191, https://doi.org/10.1016/j.rse.2014.08.029, 2014.

811 Shepherd, A., Ivins, E., Rignot, E., Smith, B., van den Broeke, M., Velicogna, I., Whitehouse, P., Briggs, K., Joughin, I.,

812 Krinner, G., Nowicki, S., Payne, T., Scambos, T., Schlegel, N., A, G., Agosta, C., Ahlstrøm, A., Babonis, G., Barletta, V. R.,

813 Bjørk, A. A., Blazquez, A., Bonin, J., Colgan, W., Csatho, B., Cullather, R., Engdahl, M. E., Felikson, D., Fettweis, X.,

814 Forsberg, R., Hogg, A. E., Gallee, H., Gardner, A., Gilbert, L., Gourmelen, N., Groh, A., Gunter, B., Hanna, E., Harig, C.,

815 Helm, V., Horvath, A., Horwath, M., Khan, S., Kjeldsen, K. K., Konrad, H., Langen, P. L., Lecavalier, B., Loomis, B., Luthcke,

816 S., McMillan, M., Melini, D., Mernild, S., Mohajerani, Y., Moore, P., Mottram, R., Mouginot, J., Moyano, G., Muir, A.,

817 Nagler, T., Nield, G., Nilsson, J., Noël, B., Otosaka, I., Pattle, M. E., Peltier, W. R., Pie, N., Rietbroek, R., Rott, H.,

818 Sandberg Sørensen, L., Sasgen, I., Save, H., Scheuchl, B., Schrama, E., Schröder, L., Seo, K. W., Simonsen, S. B., Slater, T.,

819 Spada, G., Sutterley, T., Talpe, M., Tarasov, L., van de Berg, W. J., van der Wal, W., van Wessem, M., Vishwakarma, B. D.,

820 Wiese, D., Wilton, D., Wagner, T., Wouters, B., and Wuite, J.: Mass balance of the Greenland Ice Sheet from 1992 to 2018,

821 Nature, 579, 233–239, https://doi.org/10.1038/s41586-019-1855-2, 2020.

822 Smith, L. C., Yang, K., Pitcher, L. H., Overstreet, B. T., Chu, V. W., Rennermalm, Å. K., Ryan, J. C., Cooper, M. G., Gleason,

823   C. J., Tedesco, M., Jeyaratnam, J., Van As, D., Van Den Broeke, M. R., Van De Berg, W. J., Noël, B., Langen, P. L., Cullather,

824   R. I., Zhao, B., Willis, M. J., Hubbard, A., Box, J. E., Jenner, B. A., and Behar, A. E.: Direct measurements of meltwater runoff

825   on the Greenland ice sheet surface, Proc. Natl. Acad. Sci. U. S. A., 114, E10622–E10631,

826   https://doi.org/10.1073/pnas.1707743114, 2017.

827   Steffen, K. and Box, J. E.: Surface climatology of the Greenland ice sheet : Overview of study area . Monthly mean sea level

828   pressure fields for (b) January , November the National Centers for Environmental Prediction, J. Geophys. Res., 106, 33951–

829   33964, 2001.

830   Steffen, K., Box, J. E., and Abdalati, W.: Greenland climate network: GC-Net, US Army Cold Reg. Reatt. Eng. (CRREL),

831   CRREL Spec. Rep., 98–103, 1996.

832   Steger, C. R., Reijmer, C. H., and Van Den Broeke, M. R.: The modelled liquid water balance of the Greenland Ice Sheet,

833   Cryosphere, 11, 2507–2526, https://doi.org/10.5194/tc-11-2507-2017, 2017.

834   Sturm, M., Holmgren, J., König, M., and Morris, K.: The thermal conductivity of seasonal snow, J. Glaciol., 43, 26–41,

835   https://doi.org/10.1017/S0022143000002781, 1997.

836   Sundal, A. V., Shepherd, A., Nienow, P., Hanna, E., Palmer, S., and Huybrechts, P.: Melt-induced speed-up of Greenland ice

837   sheet offset by efficient subglacial drainage, Nature, 469, 521–524, https://doi.org/10.1038/nature09740, 2011.

838   Tedesco, M.: Snowmelt detection over the Greenland ice sheet from SSM/I brightness temperature daily variations, Geophys.

839   Res. Lett., 34, 1–6, https://doi.org/10.1029/2006GL028466, 2007.

840   Tedesco, M.: Assessment and development of snowmelt retrieval algorithms over Antarctica from K-band spaceborne

841   brightness temperature (1979-2008), Remote Sens. Environ., 113, 979–997, https://doi.org/10.1016/j.rse.2009.01.009, 2009.

842   Tedesco, M., Abdalati, W., and Zwally, H. J.: Persistent surface snowmelt over Antarctica (1987-2006) from 19.35 GHz

843   brightness temperatures, Geophys. Res. Lett., 34, 1–6, https://doi.org/10.1029/2007GL031199, 2007.

844   Tedstone, A. J. and Machguth, H.: Increasing surface runoff from Greenland's firn areas, Nat. Clim. Chang., 12, 672–676,

845   https://doi.org/10.1038/s41558-022-01371-z, 2022.

846   Thompson-Munson, M., Wever, N., Stevens, C. M., Lenaerts, J. T. M., and Medley, B.: An evaluation of a physics-based firn

847   model and a semi-empirical firn model across the Greenland Ice Sheet (1980-2020), Cryosphere, 17, 2185–2209,

848   https://doi.org/10.5194/tc-17-2185-2023, 2023.

849   Tsang, L., Chen, C.-T., Chang, A. T. C., Guo, J., and Ding, K.-H.: Dense media radiative transfer theory based on

850   quasicrystalline approximation with applications to passive microwave remote sensing of snow, Radio Sci., 35, 731–749,

851   https://doi.org/https://doi.org/10.1029/1999RS002270, 2000.

852   Ulaby, F. and Long, D.: Microwave Radar and Radiometric Remote Sensing, Microw. Radar Radiom. Remote Sens.,

853   https://doi.org/10.3998/0472119356, 2014.

854   Vandecrux, B., MacFerrin, M., MacHguth, H., Colgan, W. T., Van As, D., Heilig, A., Max Stevens, C., Charalampidis, C.,

855   Fausto, R. S., Morris, E. M., Mosley-Thompson, E., Koenig, L., Montgomery, L. N., Miège, C., Simonsen, S. B., Ingeman-

856   Nielsen, T., and Box, J. E.: Firn data compilation reveals widespread decrease of firn air content in western Greenland,

857 Cryosphere, 13, 845–859, https://doi.org/10.5194/tc-13-845-2019, 2019.

858 Vandecrux, B., Mottram, R., L. Langen, P., S. Fausto, R., Olesen, M., Max Stevens, C., Verjans, V., Leeson, A., Ligtenberg,
859 S., Kuipers Munneke, P., Marchenko, S., Van Pelt, W., R. Meyer, C., B. Simonsen, S., Heilig, A., Samimi, S., Marshall, S.,
860 MacHguth, H., MacFerrin, M., Niwano, M., Miller, O., I. Voss, C., and E. Box, J.: The firn meltwater Retention Model
861 Intercomparison Project (RetMIP): Evaluation of nine firn models at four weather station sites on the Greenland ice sheet,
862 Cryosphere, 14, 3785–3810, https://doi.org/10.5194/tc-14-3785-2020, 2020.

863 Vandecrux, B., Box, J. E., Wehrlé, A., Kokhanovsky, A. A., Picard, G., Niwano, M., Hörhold, M., Faber, A. K., and Steen-
864 Larsen, H. C.: The Determination of the Snow Optical Grain Diameter and Snowmelt Area on the Greenland Ice Sheet Using
865 Spaceborne Optical Observations, Remote Sens., 14, https://doi.org/10.3390/rs14040932, 2022.

866 Vandecrux, B., Fausto, R. S., Box, J. E., Covi, F., Hock, R., Rennermalm, A. K., Heilig, A., Abermann, J., Van As, D., Bjerre,
867 E., Fettweis, X., Smeets, P. C. J. P., Kuipers Munneke, P., Van Den Broeke, M. R., Brils, M., Langen, P. L., Mottram, R., and
868 Ahlstrøm, A. P.: Historical snow and ice temperature observations document the recent warming of the Greenland ice sheet,
869 1985, 609–631, 2023a.

870 Vandecrux, B., Amory, C., Ahlstrøm, A. P., Akers, P. D., Albert, M., Alley, B., Arnaud, L., Bales, R., Benson, C., Box, J. E.,
871 Buizert, C., Charalampidis, C., Clerx, N., Covi, F., Denis, G., Dibb, J. E., Ding, M., Eisen, O., Fausto, R., Fernandoy, F.,
872 Freitag, J., Niwano, M., Osterberg, E., Otosaka, I., Picard, G., and Rennermalm, A.: The SUMup collaborative database :
873 Surface mass balance , subsurface temperature and density measurements from the Greenland and Antarctic ice sheets, 1–58
874 pp., 2023b.

875 Verjans, V., Leeson, A. A., Max Stevens, C., MacFerrin, M., Noël, B., and Van Den Broeke, M. R.: Development of physically
876 based liquid water schemes for Greenland firn-densification models, Cryosphere, 13, 1819–1842, https://doi.org/10.5194/tc-
877 13-1819-2019, 2019.

878 Vionnet, V., Brun, E., Morin, S., Boone, A., Faroux, S., Le Moigne, P., Martin, E., and Willemet, J. M.: The detailed snowpack
879 scheme Crocus and its implementation in SURFEX v7.2, Geosci. Model Dev., 5, 773–791, https://doi.org/10.5194/gmd-5-
880 773-2012, 2012.

881 Wismann, V.: Monitoring of seasonal snowmelt on Greenland with ERS scatterometer data, IEEE Trans. Geosci. Remote
882 Sens., 38, 1821–1826, https://doi.org/10.1109/36.851766, 2000.

883 Zeiger, P., Picard, G., Richaume, P., and Mialon, A.: Remote Sensing of Environment Resolution enhancement of SMOS
884 brightness temperatures : Application to melt detection on the Antarctic and Greenland ice sheets, Remote Sens. Environ., 315,
885 114469, https://doi.org/10.1016/j.rse.2024.114469, 2024.

886 Zwally, H. J. and Fiegles, S.: Extent and duration of Antarctic surface melting, J. Glaciol., 40, 463–476,
887 https://doi.org/10.3189/s0022143000012338, 1994.

888 Zwally, H. J., Abdalati, W., Herring, T., Larson, K., Saba, J., and Steffen, K.: Surface Melt – Induced Acceleration of
889 Greenland Ice-Sheet Flow, 297, 218–222, 2002.

890